

The $e^+e^- \rightarrow \pi^+\pi^-\pi^+\pi^-$, $K^+K^-\pi^+\pi^-$, and $K^+K^-K^+K^-$ Cross Sections at Center-of-Mass Energies 0.5–4.5 GeV Measured with Initial-State Radiation

B. Aubert, R. Barate, D. Boutigny, F. Couderc, Y. Karyotakis, J. P. Lees, V. Poireau, V. Tisserand, and A. Zghiche
Laboratoire de Physique des Particules, F-74941 Annecy-le-Vieux, France

E. Grauges-Pous
IFAE, Universitat Autònoma de Barcelona, E-08193 Bellaterra, Barcelona, Spain

A. Palano and A. Pompili
Università di Bari, Dipartimento di Fisica and INFN, I-70126 Bari, Italy

J. C. Chen, N. D. Qi, G. Rong, P. Wang, and Y. S. Zhu
Institute of High Energy Physics, Beijing 100039, China

G. Eigen, I. Ofte, and B. Stugu
University of Bergen, Inst. of Physics, N-5007 Bergen, Norway

G. S. Abrams, A. W. Borgland, A. B. Breon, D. N. Brown, J. Button-Shafer, R. N. Cahn,
E. Charles, C. T. Day, M. S. Gill, A. V. Gritsan, Y. Groysman, R. G. Jacobsen, R. W. Kadel,
J. Kadyk, L. T. Kerth, Yu. G. Kolomensky, G. Kukartsev, G. Lynch, L. M. Mir,
P. J. Oddone, T. J. Orimoto, M. Pripstein, N. A. Roe, M. T. Ronan, and W. A. Wenzel
Lawrence Berkeley National Laboratory and University of California, Berkeley, California 94720, USA

M. Barrett, K. E. Ford, T. J. Harrison, A. J. Hart, C. M. Hawkes, S. E. Morgan, and A. T. Watson
University of Birmingham, Birmingham, B15 2TT, United Kingdom

M. Fritsch, K. Goetzen, T. Held, H. Koch, B. Lewandowski, M. Pelizaeus, K. Peters, T. Schroeder, and M. Steinke
Ruhr Universität Bochum, Institut für Experimentalphysik 1, D-44780 Bochum, Germany

J. T. Boyd, J. P. Burke, N. Chevalier, W. N. Cottingham, M. P. Kelly, T. E. Latham, and F. F. Wilson
University of Bristol, Bristol BS8 1TL, United Kingdom

T. Cuhadar-Donszelmann, C. Hearty, N. S. Knecht, T. S. Mattison, J. A. McKenna, and D. Thiessen
University of British Columbia, Vancouver, British Columbia, Canada V6T 1Z1

A. Khan, P. Kyberd, and L. Teodorescu
Brunel University, Uxbridge, Middlesex UB8 3PH, United Kingdom

A. E. Blinov, V. E. Blinov, V. P. Druzhinin, V. B. Golubev, V. N. Ivanchenko, E. A. Kravchenko,
A. P. Onuchin, S. I. Serednyakov, Yu. I. Skovpen, E. P. Solodov, and A. N. Yushkov
Budker Institute of Nuclear Physics, Novosibirsk 630090, Russia

D. Best, M. Bruinsma, M. Chao, I. Eschrich, D. Kirkby, A. J. Lankford,
M. Mandelkern, R. K. Mommsen, W. Roethel, and D. P. Stoker
University of California at Irvine, Irvine, California 92697, USA

C. Buchanan, B. L. Hartfiel, and A. J. R. Weinstein
University of California at Los Angeles, Los Angeles, California 90024, USA

S. D. Foulkes, J. W. Gary, O. Long, B. C. Shen, and K. Wang
University of California at Riverside, Riverside, California 92521, USA

D. del Re, H. K. Hadavand, E. J. Hill, D. B. MacFarlane, H. P. Paar, Sh. Rahatlou, and V. Sharma
University of California at San Diego, La Jolla, California 92093, USA

J. W. Berryhill, C. Campagnari, A. Cunha, B. Dahmes,
T. M. Hong, A. Lu, M. A. Mazur, J. D. Richman, and W. Verkerke
University of California at Santa Barbara, Santa Barbara, California 93106, USA

T. W. Beck, A. M. Eisner, C. J. Flacco, C. A. Heusch, J. Kroseberg, W. S. Lockman, G. Nesom,
T. Schalk, B. A. Schumm, A. Seiden, P. Spradlin, D. C. Williams, and M. G. Wilson
University of California at Santa Cruz, Institute for Particle Physics, Santa Cruz, California 95064, USA

J. Albert, E. Chen, G. P. Dubois-Felsmann, A. Dvoretzskii, D. G. Hitlin,
I. Narsky, T. Piatenko, F. C. Porter, A. Ryd, A. Samuel, and S. Yang
California Institute of Technology, Pasadena, California 91125, USA

S. Jayatilke, G. Mancinelli, B. T. Meadows, and M. D. Sokoloff
University of Cincinnati, Cincinnati, Ohio 45221, USA

F. Blanc, P. Bloom, S. Chen, W. T. Ford, U. Nauenberg, A. Olivas,
P. Rankin, W. O. Ruddick, J. G. Smith, K. A. Ulmer, J. Zhang, and L. Zhang
University of Colorado, Boulder, Colorado 80309, USA

A. Chen, E. A. Eckhart, J. L. Harton, A. Soffer, W. H. Toki, R. J. Wilson, and Q. Zeng
Colorado State University, Fort Collins, Colorado 80523, USA

B. Spaan
Universität Dortmund, Institut für Physik, D-44221 Dortmund, Germany

D. Altenburg, T. Brandt, J. Brose, M. Dickopp, E. Feltresi, A. Hauke, H. M. Lacker, E. Maly, R. Nogowski,
S. Otto, A. Petzold, G. Schott, J. Schubert, K. R. Schubert, R. Schwierz, and J. E. Sundermann
Technische Universität Dresden, Institut für Kern- und Teilchenphysik, D-01062 Dresden, Germany

D. Bernard, G. R. Bonneaud, P. Grenier, S. Schrenk, Ch. Thiebaux, G. Vasileiadis, and M. Verderi
Ecole Polytechnique, LLR, F-91128 Palaiseau, France

D. J. Bard, P. J. Clark, F. Muheim, S. Playfer, and Y. Xie
University of Edinburgh, Edinburgh EH9 3JZ, United Kingdom

M. Andreotti, V. Azzolini, D. Bettoni, C. Bozzi, R. Calabrese,
G. Cibinetto, E. Luppi, M. Negrini, L. Piemontese, and A. Sarti
Università di Ferrara, Dipartimento di Fisica and INFN, I-44100 Ferrara, Italy

F. Anulli, R. Baldini-Ferrolì, A. Calcaterra, R. de Sangro,
G. Finocchiaro, P. Patteri, I. M. Peruzzi, M. Piccolo, and A. Zallo
Laboratori Nazionali di Frascati dell'INFN, I-00044 Frascati, Italy

A. Buzzo, R. Capra, R. Contri, G. Crosetti, M. Lo Vetere, M. Macri,
M. R. Monge, S. Passaggio, C. Patrignani, E. Robutti, A. Santroni, and S. Tosi
Università di Genova, Dipartimento di Fisica and INFN, I-16146 Genova, Italy

S. Bailey, G. Brandenburg, K. S. Chaisanguanthum, M. Morii, and E. Won
Harvard University, Cambridge, Massachusetts 02138, USA

R. S. Dubitzky, U. Langenegger, J. Marks, and U. Uwer
Universität Heidelberg, Physikalisches Institut, Philosophenweg 12, D-69120 Heidelberg, Germany

W. Bhimji, D. A. Bowerman, P. D. Dauncey, U. Egede, J. R. Gaillard,
G. W. Morton, J. A. Nash, M. B. Nikolich, and G. P. Taylor
Imperial College London, London, SW7 2AZ, United Kingdom

M. J. Charles, G. J. Grenier, U. Mallik, and A. K. Mohapatra
University of Iowa, Iowa City, Iowa 52242, USA

J. Cochran, H. B. Crawley, J. Lamsa, W. T. Meyer, S. Prell, E. I. Rosenberg, A. E. Rubin, and J. Yi
Iowa State University, Ames, Iowa 50011-3160, USA

N. Arnaud, M. Davier, X. Giroux, G. Grosdidier, A. Höcker, F. Le Diberder, V. Lepeltier,
 A. M. Lutz, T. C. Petersen, M. Pierini, S. Plaszczynski, M. H. Schune, and G. Wormser
Laboratoire de l'Accélérateur Linéaire, F-91898 Orsay, France

C. H. Cheng, D. J. Lange, M. C. Simani, and D. M. Wright
Lawrence Livermore National Laboratory, Livermore, California 94550, USA

A. J. Bevan, C. A. Chavez, J. P. Coleman, I. J. Forster, J. R. Fry, E. Gabathuler,
 R. Gamet, D. E. Hutchcroft, R. J. Parry, D. J. Payne, and C. Touramanis
University of Liverpool, Liverpool L69 72E, United Kingdom

C. M. Cormack and F. Di Lodovico
Queen Mary, University of London, E1 4NS, United Kingdom

C. L. Brown, G. Cowan, R. L. Flack, H. U. Flaecher, M. G. Green,
 P. S. Jackson, T. R. McMahon, S. Ricciardi, F. Salvatore, and M. A. Winter
University of London, Royal Holloway and Bedford New College, Egham, Surrey TW20 0EX, United Kingdom

D. Brown and C. L. Davis
University of Louisville, Louisville, Kentucky 40292, USA

J. Allison, N. R. Barlow, R. J. Barlow, M. C. Hodgkinson, G. D. Lafferty, M. T. Naisbit, and J. C. Williams
University of Manchester, Manchester M13 9PL, United Kingdom

C. Chen, A. Farbin, W. D. Hulsbergen, A. Jawahery, D. Kovalskyi, C. K. Lae, V. Lillard, and D. A. Roberts
University of Maryland, College Park, Maryland 20742, USA

G. Blaylock, C. Dallapiccola, S. S. Hertzbach, R. Kofler,
 V. B. Koptchev, T. B. Moore, S. Saremi, H. Staengle, and S. Willocq
University of Massachusetts, Amherst, Massachusetts 01003, USA

R. Cowan, K. Koeneke, G. Sciolla, S. J. Sekula, F. Taylor, and R. K. Yamamoto
Massachusetts Institute of Technology, Laboratory for Nuclear Science, Cambridge, Massachusetts 02139, USA

P. M. Patel and S. H. Robertson
McGill University, Montréal, Quebec, Canada H3A 2T8

A. Lazzaro, V. Lombardo, and F. Palombo
Università di Milano, Dipartimento di Fisica and INFN, I-20133 Milano, Italy

J. M. Bauer, L. Cremaldi, V. Eschenburg, R. Godang, R. Kroeger,
 J. Reidy, D. A. Sanders, D. J. Summers, and H. W. Zhao
University of Mississippi, University, Mississippi 38677, USA

S. Brunet, D. Côté, and P. Taras
Université de Montréal, Laboratoire René J. A. Lévesque, Montréal, Quebec, Canada H3C 3J7

H. Nicholson
Mount Holyoke College, South Hadley, Massachusetts 01075, USA

N. Cavallo,* F. Fabozzi,* C. Gatto, L. Lista, D. Monorchio, P. Paolucci, D. Piccolo, and C. Sciacca
Università di Napoli Federico II, Dipartimento di Scienze Fisiche and INFN, I-80126, Napoli, Italy

M. Baak, H. Bulten, G. Raven, H. L. Snoek, and L. Wilden
NIKHEF, National Institute for Nuclear Physics and High Energy Physics, NL-1009 DB Amsterdam, The Netherlands

C. P. Jessop and J. M. LoSecco
University of Notre Dame, Notre Dame, Indiana 46556, USA

T. Allmendinger, G. Benelli, K. K. Gan, K. Honscheid, D. Hufnagel, H. Kagan,
 R. Kass, T. Pulliam, A. M. Rahimi, R. Ter-Antonyan, and Q. K. Wong
Ohio State University, Columbus, Ohio 43210, USA

J. Brau, R. Frey, O. Igonkina, M. Lu, C. T. Potter, N. B. Sinev, D. Strom, and E. Torrence
University of Oregon, Eugene, Oregon 97403, USA

F. Colecchia, A. Dorigo, F. Galeazzi, M. Margoni, M. Morandin,
 M. Posocco, M. Rotondo, F. Simonetto, R. Stroili, and C. Voci
Università di Padova, Dipartimento di Fisica and INFN, I-35131 Padova, Italy

M. Benayoun, H. Briand, J. Chauveau, P. David, L. Del Buono, Ch. de la Vaissière,
 O. Hamon, M. J. J. John, Ph. Leruste, J. Malclès, J. Ocariz, L. Roos, and G. Therin
Universités Paris VI et VII, Laboratoire de Physique Nucléaire et de Hautes Energies, F-75252 Paris, France

P. K. Behera, L. Gladney, Q. H. Guo, and J. Panetta
University of Pennsylvania, Philadelphia, Pennsylvania 19104, USA

M. Biasini, R. Covarelli, and M. Pioppi
Università di Perugia, Dipartimento di Fisica and INFN, I-06100 Perugia, Italy

C. Angelini, G. Batignani, S. Bettarini, M. Bondioli, F. Bucci, G. Calderini, M. Carpinelli, F. Forti, M. A. Giorgi,
 A. Lusiani, G. Marchiori, M. Morganti, N. Neri, E. Paoloni, M. Rama, G. Rizzo, G. Simi, and J. Walsh
Università di Pisa, Dipartimento di Fisica, Scuola Normale Superiore and INFN, I-56127 Pisa, Italy

M. Haire, D. Judd, K. Paick, and D. E. Wagoner
Prairie View A&M University, Prairie View, Texas 77446, USA

N. Danielson, P. Elmer, Y. P. Lau, C. Lu, V. Miftakov, J. Olsen, A. J. S. Smith, and A. V. Telnov
Princeton University, Princeton, New Jersey 08544, USA

F. Bellini, A. D'Orazio, E. Di Marco, R. Faccini, F. Ferrarotto, F. Ferroni, M. Gaspero, L. Li
 Gioi, M. A. Mazzoni, S. Morganti, G. Piredda, F. Polci, F. Safai Tehrani, and C. Voena
Università di Roma La Sapienza, Dipartimento di Fisica and INFN, I-00185 Roma, Italy

G. Cavoto
Princeton University, Princeton, New Jersey 08544, USA and
Università di Roma La Sapienza, Dipartimento di Fisica and INFN, I-00185 Roma, Italy

S. Christ, H. Schröder, G. Wagner, and R. Waldi
Universität Rostock, D-18051 Rostock, Germany

T. Adye, N. De Groot, B. Franek, G. P. Gopal, and E. O. Olaiya
Rutherford Appleton Laboratory, Chilton, Didcot, Oxon, OX11 0QX, United Kingdom

R. Aleksan, S. Emery, A. Gaidot, S. F. Ganzhur, P.-F. Giraud, G. Graziani, G. Hamel de Monchenault,
 W. Kozanecki, M. Legendre, G. W. London, B. Mayer, G. Vasseur, Ch. Yèche, and M. Zito
DSM/Daphnia, CEA/Saclay, F-91191 Gif-sur-Yvette, France

M. V. Purohit, A. W. Weidemann, J. R. Wilson, and F. X. Yumiceva
University of South Carolina, Columbia, South Carolina 29208, USA

T. Abe, D. Aston, R. Bartoldus, N. Berger, A. M. Boyarski, O. L. Buchmueller, R. Claus, M. R. Convery, M. Cristinziani, G. De Nardo, J. C. Dingfelder, D. Dong, J. Dorfan, D. Dujmic, W. Dunwoodie, S. Fan, R. C. Field, T. Glanzman, S. J. Gowdy, T. Hadig, V. Halyo, C. Hast, T. Hryn'ova, W. R. Innes, M. H. Kelsey, P. Kim, M. L. Kocian, D. W. G. S. Leith, J. Libby, S. Luitz, V. Luth, H. L. Lynch, H. Marsiske, R. Messner, D. R. Muller, C. P. O'Grady, V. E. Ozcan, A. Perazzo, M. Perl, B. N. Ratcliff, A. Roodman, A. A. Salnikov, R. H. Schindler, J. Schwiening, A. Snyder, A. Soha, J. Stelzer, D. Su, M. K. Sullivan, J. Va'vra, S. R. Wagner, M. Weaver, W. J. Wisniewski, M. Wittgen, D. H. Wright, A. K. Yarritu, and C. C. Young
Stanford Linear Accelerator Center, Stanford, California 94309, USA

J. Strube
*University of Oregon, Eugene, Oregon 97403, USA and
Stanford Linear Accelerator Center, Stanford, California 94309, USA*

P. R. Burchat, A. J. Edwards, S. A. Majewski, B. A. Petersen, and C. Roat
Stanford University, Stanford, California 94305-4060, USA

M. Ahmed, S. Ahmed, M. S. Alam, J. A. Ernst, M. A. Saeed, M. Saleem, and F. R. Wappler
State University of New York, Albany, New York 12222, USA

W. Bugg, M. Krishnamurthy, and S. M. Spanier
University of Tennessee, Knoxville, Tennessee 37996, USA

R. Eckmann, H. Kim, J. L. Ritchie, A. Satpathy, and R. F. Schwitters
University of Texas at Austin, Austin, Texas 78712, USA

J. M. Izen, I. Kitayama, X. C. Lou, and S. Ye
University of Texas at Dallas, Richardson, Texas 75083, USA

F. Bianchi, M. Bona, F. Gallo, and D. Gamba
Università di Torino, Dipartimento di Fisica Sperimentale and INFN, I-10125 Torino, Italy

L. Bosisio, C. Cartaro, F. Cossutti, G. Della Ricca, S. Dittongo, S. Grancagnolo, L. Lanceri, P. Poropat,[†] L. Vitale, and G. Vuagnin
Università di Trieste, Dipartimento di Fisica and INFN, I-34127 Trieste, Italy

F. Martinez-Vidal
*IFAE, Universitat Autònoma de Barcelona, E-08193 Bellaterra, Barcelona, Spain and
IFIC, Universitat de Valencia-CSIC, E-46071 Valencia, Spain*

R. S. Panvini[†]
Vanderbilt University, Nashville, Tennessee 37235, USA

Sw. Banerjee, B. Bhuyan, C. M. Brown, D. Fortin, K. Hamano, P. D. Jackson, R. Kowalewski, J. M. Roney, and R. J. Sobie
University of Victoria, Victoria, British Columbia, Canada V8W 3P6

J. J. Back, P. F. Harrison, and G. B. Mohanty
Department of Physics, University of Warwick, Coventry CV4 7AL, United Kingdom

H. R. Band, X. Chen, B. Cheng, S. Dasu, M. Datta, A. M. Eichenbaum, K. T. Flood, M. Graham, J. J. Hollar, J. R. Johnson, P. E. Kutter, H. Li, R. Liu, A. Mihalysi, Y. Pan, R. Prepost, P. Tan, J. H. von Wimmersperg-Toeller, J. Wu, S. L. Wu, and Z. Yu
University of Wisconsin, Madison, Wisconsin 53706, USA

M. G. Greene and H. Neal
Yale University, New Haven, Connecticut 06511, USA

(Dated: October 24, 2018)

We study the process $e^+e^- \rightarrow \pi^+\pi^-\pi^+\pi^-\gamma$, with a hard photon radiated from the initial state. About 60,000 fully reconstructed events have been selected from 89 fb^{-1} of *BABAR* data. The invariant mass of the hadronic final state defines the effective e^+e^- center-of-mass energy, so that these data can be compared with the corresponding direct e^+e^- measurements. From the 4π -mass spectrum, the cross section for the process $e^+e^- \rightarrow \pi^+\pi^-\pi^+\pi^-$ is measured for center-of-mass energies from 0.6 to 4.5 GeV. The uncertainty in the cross section measurement is typically 5%. We also measure the cross sections for the final states $K^+K^-\pi^+\pi^-$ and $K^+K^-K^+K^-$. We observe the J/ψ in all three final states and measure the corresponding branching fractions. We search for $X(3872)$ in $J/\psi(\rightarrow \mu^+\mu^-)\pi^+\pi^-$ and obtain an upper limit on the product of the e^+e^- width of the $X(3872)$ and the branching fraction for $X(3872) \rightarrow J/\psi\pi^+\pi^-$.

PACS numbers: 13.66.Bc, 14.40.Cs, 13.25.Gv, 13.25.Jx, 13.20.Jf

I. INTRODUCTION

The idea of utilizing initial-state radiation (ISR) from a high-mass state to explore electron-positron processes at all energies below that state was outlined in Ref. [1]. The possibility of exploiting such processes in high luminosity ϕ - and B -factories was discussed in Refs. [2–4] and motivates the study described in this paper. This is of particular interest because of the small discrepancy between the measured muon $g-2$ value and that predicted by the Standard Model [5], where hadronic loop contributions are obtained from e^+e^- experiments at low center-of-mass (c.m.) energies. The study of ISR events at B -factories provides independent and contiguous measurements of hadronic cross sections in this energy region and also contributes to the investigation of low-mass resonance spectroscopy.

The ISR cross section for a particular hadronic final state f (excluding the radiated photon) is related to the corresponding e^+e^- cross section $\sigma_f(s)$ by:

$$\frac{d\sigma_f(s, x)}{dx} = W(s, x) \cdot \sigma_f(s(1-x)), \quad (1)$$

where $x = 2E_\gamma/\sqrt{s}$; E_γ is the energy of the ISR photon in the nominal e^+e^- c.m. frame; \sqrt{s} is the nominal e^+e^- c.m. energy; and $\sqrt{s(1-x)}$ is the effective c.m. energy at which the final state f is produced. The function

$$W(s, x) = \beta \cdot \left[(1 + \delta) \cdot x^{(\beta-1)} - 1 + \frac{x}{2} \right] \quad (2)$$

(see for example Ref. [4]) describes the energy spectrum of the ISR photons, where $\beta = 2\alpha/\pi \cdot (2\ln(\sqrt{s}/m_e) - 1)$ and δ takes into account vertex and self-energy corrections. At the $\Upsilon(4S)$ energy, 10.58 GeV, $\beta = 0.088$ and $\delta = 0.067$. ISR photons are produced at all angles. For the present study it is required that the hard ISR photon be detected in the electromagnetic calorimeter (EMC) of the *BABAR* detector. Our acceptance for such photons is 10–15% [4].

Events corresponding to $e^+e^- \rightarrow \mu^+\mu^-\gamma$ provide the ISR-luminosity normalization for the hadronic cross section measurements. For a hadronic final state f , the Born cross section at center-of-mass energy squared s' , $\sigma_f(s')$, is obtained by relating the observed number of events, $dN_{f\gamma}$, in an interval ds' centered at s' , to the corresponding number of radiative di-muon events, $dN_{\mu\mu\gamma}$, by means of

$$\sigma_f(s') = \frac{dN_{f\gamma} \cdot \epsilon_{\mu\mu} \cdot (1 + \delta_{\text{FSR}}^{\mu\mu})}{dN_{\mu\mu\gamma} \cdot \epsilon_f \cdot (1 + \delta_{\text{FSR}}^f)} \cdot \sigma_{e^+e^- \rightarrow \mu^+\mu^-}(s'). \quad (3)$$

Here $s' \equiv s(1-x)$, $\epsilon_{\mu\mu}$ and ϵ_f are detection efficiencies, and $(1 + \delta_{\text{FSR}}^{\mu\mu})$ and $(1 + \delta_{\text{FSR}}^f)$ are corrections for the possibility that the detected hard photon may be the result of final-state radiation (FSR). This correction is important for di-muon events, but is negligible for most hadronic final states. The Born cross section $\sigma_{e^+e^- \rightarrow \mu^+\mu^-}(s')$ is used. The radiative corrections to the initial state, the acceptance for the ISR photon, and the virtual photon properties are the same for $\mu^+\mu^-$ and f , and cancel in the ratio.

An important advantage of ISR data is that the entire range of effective c.m. energies is scanned in one experiment. This avoids the relative normalization uncertainties that inevitably arise when data from different experiments, or from different machine settings, are combined.

A disadvantage of the ISR measurement is that the mass resolution is much poorer than can be obtained in a direct annihilation. The resolution and absolute energy scale can be monitored directly by the width and mass of the J/ψ resonance produced in the reaction $e^+e^- \rightarrow J/\psi\gamma$. By using a kinematic fit to this reaction, we find the resolution to be about 8 MeV/ c^2 for decays of J/ψ in the $\mu^+\mu^-$ mode [7].

Preliminary studies of $e^+e^- \rightarrow \mu^+\mu^-\gamma$ and some multihadron ISR processes have been performed with *BABAR* data [6–8]. These demonstrated good detector efficiency and particle identification capability for events of this kind.

This paper reports analyses of the $\pi^+\pi^-\pi^+\pi^-$, $K^+K^-\pi^+\pi^-$ and $K^+K^-K^+K^-$ final states produced in conjunction with a hard photon, assumed to result from ISR. While *BABAR* data are available at effective c.m. energies up to 10.58 GeV, the present analysis is restricted to energies below 4.5 GeV because of backgrounds from

*Also with Università della Basilicata, Potenza, Italy

†Deceased

$\Upsilon(4S)$ decays. A clear J/ψ signal is observed for each of these hadronic states and the corresponding J/ψ branching fractions are measured. A search for the $X(3872)\gamma$ process with the $X(3872)$ decay to $J/\psi\pi^+\pi^-$ is also carried out.

II. THE BABAR DETECTOR AND DATASET

The data used in this analysis were collected with the BABAR detector at the PEP-II asymmetric e^+e^- storage ring. The total integrated luminosity used is 89 fb^{-1} , which includes data collected at the $\Upsilon(4S)$ resonance mass (80 fb^{-1}), and at c.m. energy 40 MeV lower (9 fb^{-1}).

The BABAR detector is described elsewhere [9]. Final states with four charged particles are reconstructed in the BABAR tracking system, which comprises the Silicon Vertex Tracker (SVT) and the drift chamber (DCH). Separation of pions and kaons is accomplished by means of the Detector of Internally Reflected Cherenkov Light (DIRC) and energy-loss measurements in the SVT and DCH. The hard photon is detected in the EMC. Muon identification is provided by the Instrumented Flux Return (IFR) and this information is used to select the $\mu^+\mu^-\gamma$ final state and in the $X(3872)$ search.

The initial selection of candidate events requires that a high-energy photon in the event with $E_{\text{c.m.}}^\gamma > 3 \text{ GeV}$ be found recoiling against four good quality charged tracks with zero net charge. Events having such a high-energy photon together with an odd number (≥ 3) of good charged tracks are also selected, for the purpose of making estimates of the tracking efficiency. Each charged track is required to originate close to the interaction region, to have transverse momentum greater than $0.1 \text{ GeV}/c$ and to have a polar angle in the laboratory frame with respect to the collision axis in the range from 0.4 to 2.45 radians. These selections guarantee the quality of the charged tracks in the DCH. Events with electrons and positrons are removed on the basis of associated EMC-energy deposition and energy-loss (dE/dx) information from the DCH.

In order to study the detector acceptance and efficiency, we developed a special package of simulation programs for radiative processes. The simulation of the $\pi^+\pi^-\pi^+\pi^-\gamma$ final state is based on the generator developed by Kuehn and Czyz [10]. The model assumes $a_1(1260)\pi$ dominance [18, 19], so that many of the events contain a pair of pions from a ρ meson due to the decay $a_1(1260) \rightarrow \rho^0\pi$. No corresponding generator exists for the $K^+K^-\pi^+\pi^-$ and $K^+K^-K^+K^-$ final states, so these reactions were simulated according to phase space.

Multiple soft-photon emission from the initial-state charged particles is implemented with the structure-function technique [11, 12], while extra photon radiation from the final-state particles is simulated by means of the PHOTOS package [13]. The accuracy of the radiative corrections is about 1%.

A sample of about 400k events were generated with these tools and passed through the detector response simulation [14]. These events were then reconstructed through the same software chain as the experimental data. Variations in detector and background conditions were taken into account.

For purposes of background estimation, a large sample of events from the main ISR processes ($2\pi\gamma$, $3\pi\gamma$... $6\pi\gamma$, $2K\pi\gamma$...) was simulated. This sample exceeded the expected number of events in the dataset by a factor of about three. In addition, the expected numbers of $e^+e^- \rightarrow q\bar{q}$ ($q = u, d, s, c$) events were generated via JETSET [15] and $e^+e^- \rightarrow \tau^+\tau^-$ via KORALB [16] in order to estimate non-ISR-type background contributions. The cross sections for the above processes are known with about 10% accuracy or better, which is sufficient for the background contribution study.

III. THE KINEMATIC FIT PROCEDURE

The initial sample of candidate events is subjected to a constrained kinematic fit in conjunction with charged-particle identification to extract events corresponding to the final states of interest.

For each particular four-charged-particle candidate, and for each possible combination of particle types (i.e. 4π , $2K2\pi$ or $4K$), a one-constraint kinematic fit is performed without using information from the detected photon candidate. Because of the excellent resolution of the DCH, the three-momentum vector of the photon is better determined through momentum conservation than through measurement in the EMC. As a consequence, the calibration accuracy of the EMC and its alignment with respect to the DCH do not contribute to the systematic uncertainties. The initial e^+e^- and final-state charged-particle four-momenta and their covariance matrices are taken into account. The momentum vector of the photon reconstructed by the fit in the laboratory frame is required to have polar angle $\theta_\gamma^{\text{fit}}$ in the range from 0.35 to 2.4 radians and to match the measured polar angle $\theta_\gamma^{\text{meas}}$ of a candidate photon in the EMC within 50 mrad. The corresponding azimuthal angles, ϕ_γ^{fit} and $\phi_\gamma^{\text{meas}}$, are also required to agree to this same tolerance. These angular criteria reduce the background by a factor of about two with no noticeable loss of signal. Finally, the polar angle $\theta_{\text{ch}}^{\text{fit}}$ of each charged track after the fit has to satisfy $0.45 < \theta_{\text{ch}}^{\text{fit}} < 2.4$ radians in order to fall within the acceptance of the DIRC, which provides about 80% kaon identification efficiency.

The fit for the four-pion final-state hypothesis is retained for every event. If only one track is identified as a kaon, or if two oppositely-charged kaons are identified, the $K^+K^-\pi^+\pi^-$ fit is also retained. Finally, if two, three or four kaons are identified, the four-kaon fit is applied.

For events with only three charged tracks recoiling against a candidate photon, the measured four-momentum vector of the photon and its covariance ma-

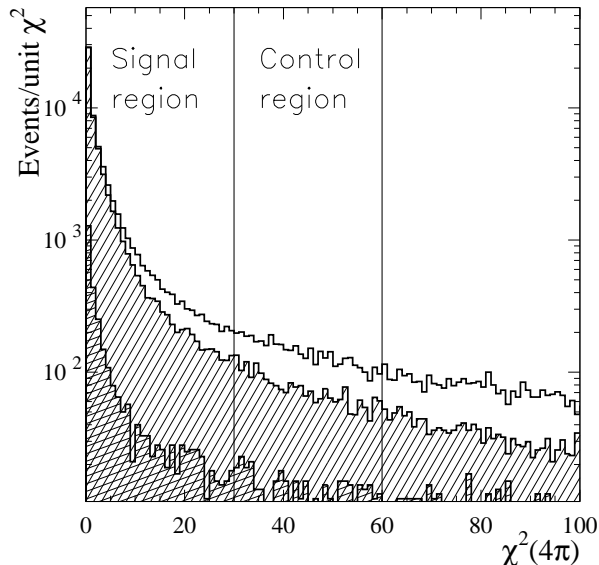


FIG. 1: The one-constraint χ^2 distributions for data (upper histogram) and MC simulation (shaded histogram) four-charged-track events fitted to the four-pion hypothesis. The cross-hatched histogram is the estimated background contribution from non-ISR events obtained from JETSET. The signal and control regions are indicated.

trix are used in a one-constraint kinematic fit which assumes, as appropriate, that only a charged pion or kaon is undetected. These events are used in the efficiency studies described below.

IV. THE $\pi^+\pi^-\pi^+\pi^-$ FINAL STATE

A. Additional selection criteria

The results of the one-constraint fit to the four charged-track candidates are used to make the final selection of the four-pion sample. We require $\chi_{4\pi}^2 < 30$ for the four-pion hypothesis, and that any accompanying fit to the $2K2\pi$ hypothesis have $\chi_{2K2\pi}^2 > 10$. We estimate that these requirements reduce the contamination of the 4π sample by $2K2\pi$ events to about 1% at the cost of about 2.4% of the signal events.

The one-constraint-fit χ^2 distribution for the four-pion candidates is shown as the upper histogram of Fig. 1, while the shaded region is for the corresponding MC-simulated pure $4\pi\gamma$ events. The experimental distribution has a contribution from the background processes but the MC-simulated distribution is also much broader than the usual one-constraint χ^2 distribution. This is due to multiple-soft-photon emission in the initial state and radiation from the final-state charged particles, neither of which is included in the constrained fit but which exist in data and MC simulation. To illustrate the difference of distributions on Fig. 1, the MC-simulated χ^2 distribution is normalized to the data in the region $\chi^2 < 1$ where

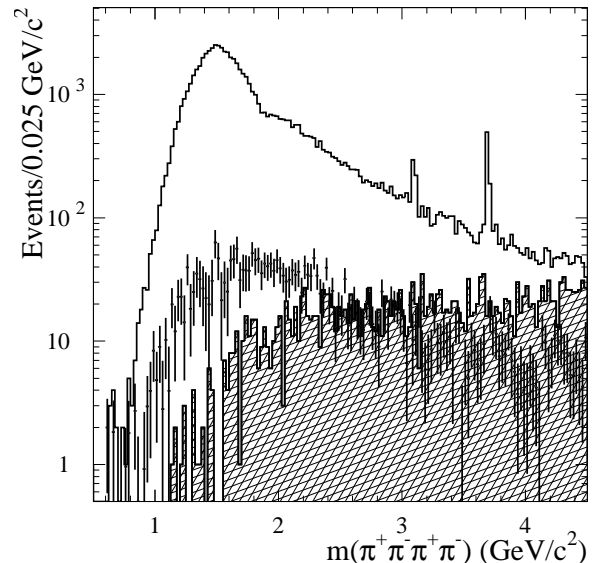


FIG. 2: The four-pion invariant mass distribution for the signal region of Fig. 1. The points indicate the background estimated from the difference between data and MC events for the control region of Fig. 1, normalized to the difference between data and MC events in the signal region of Fig. 1. The cross-hatched histogram corresponds to the non-ISR background of Fig. 1.

contamination of the background events and multiple soft ISR and FSR is lowest.

The cross-hatched histogram in Fig. 1 represents the non-ISR background contribution obtained from the JETSET simulation of quark-antiquark production and hadronization and does not exceed 3%.

The region $30 < \chi_{4\pi}^2 < 60$ is chosen as a control region for the estimation of background from other ISR and non-ISR multi-hadron reactions. The procedure followed is described in the next section.

The signal region of Fig. 1 contains 67,063 data and 71,210 MC events, while for the control region the corresponding numbers are 4,887 and 2,820 respectively.

B. Background estimation

MC simulation of the $\tau^+\tau^-$ final state and ISR production of multi-hadron final states other than $\pi^+\pi^-\pi^+\pi^-$ shows that such states would yield a background in the selected four-pion sample that would exhibit a relatively flat contribution to the $\chi_{4\pi}^2$ distribution. We subtract the shaded histograms of Fig. 1 from the plain one and the resulting histogram is well described by MC simulation of background processes. The background contribution to any distribution other than χ^2 is estimated as the difference between the distributions in the relevant quantity for data and MC events from the control region of Fig. 1, normalized to the difference between the number of data and MC events in the signal region.

For example, Fig. 2 shows the four-pion invariant mass distribution up to $4.5 \text{ GeV}/c^2$ for the signal region of Fig. 1. The points with error bars show the ISR background contribution obtained in the manner described from the control region of Fig. 1. The cross-hatched histograms in Fig. 1 and Fig. 2 represent the non-ISR background contribution obtained from the JETSET MC simulation. The χ^2 distribution for the non-ISR events is not flat, and we estimate their relative contribution to the signal region from the production cross-section and the integrated luminosity. Both backgrounds are small at low mass, but the non-ISR background accounts for almost half of the observed data at approximately $4 \text{ GeV}/c^2$. The data show a strong peak around $1.5 \text{ GeV}/c^2$ followed by a shoulder near $1.9 \text{ GeV}/c^2$. Narrow signals are apparent at the J/ψ and the $\psi(2S)$ masses, although the latter is due to $\psi(2S) \rightarrow \pi^+\pi^- J/\psi$ $J/\psi \rightarrow \mu^+\mu^-$ with the muons being treated as pions.

Accounting for uncertainties in cross sections for background processes and statistical fluctuations in the number of simulated events, we estimate that this procedure for background subtraction results in a systematic uncertainty of less than 1% in the number of signal events in the 1–3 GeV/c^2 region of four-pion mass, but that it increases to 3–5% in the region above 3 GeV/c^2 and to roughly 10% in the region below 1 GeV/c^2 .

By selecting a “background-free” $4\pi\gamma$ sample with only four charged tracks and only one photon (about 10% of events) we can compare χ^2 distributions for data and MC events up to $\chi^2 = 1000$. We estimate that for a $\chi^2_{4\pi} < 30$ selection the net signal size should be increased by $(3 \pm 2)\%$ to allow for a slight shape difference between the MC and experimental χ^2 distributions.

C. Tracking efficiency

We measure the track-finding efficiency with events that have three charged-particle tracks and a hard photon. These events are subjected to a one-constraint fit (as described in Sec. III above), which yields the three-momentum vector of the missing charged pion in the laboratory frame assuming this is the only undetected track. If the chi-squared of the fit is less than 30 and this vector lies within the acceptance of the DCH, the event is included in the data sample.

The four-pion mass distribution obtained in this way for three-charged-track events is shown in Fig. 3(a), together with the ISR (points with errors) and non-ISR (cross-hatched histogram) background estimated as described above. The behavior is similar to that observed in Fig. 2. This is exhibited explicitly in Fig. 3(b), where the ratio of the three- to four-charged track pion mass distributions (after background subtraction) is shown as a function of four-pion invariant mass for data (open points). When the MC-simulated data are treated in the same way, the solid points of Fig. 3(b) are obtained. The same absence of mass dependence is observed for data

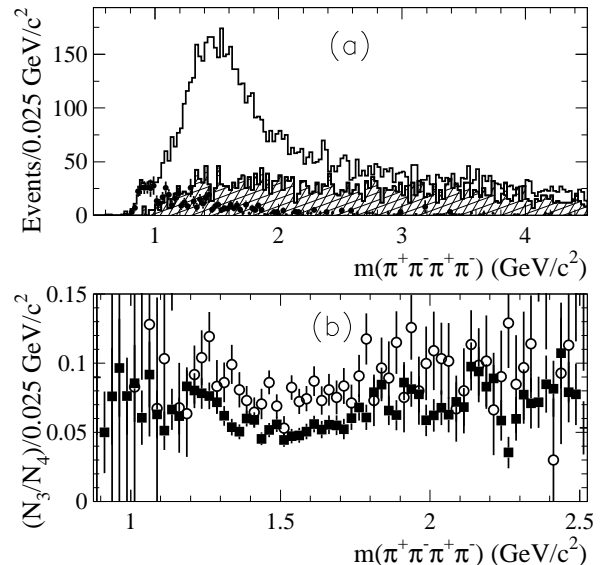


FIG. 3: (a) The four-pion invariant mass distribution obtained from fits to three-charged-track events in which an observed photon is used to constrain the unobserved fourth pion; ISR and non-ISR background contributions are indicated by the points with error bars and the cross-hatched histogram, respectively. (b) The four-pion mass dependence of the ratio between the three- and four-charged-track distributions for data (open circles) and MC simulation (solid squares).

and MC events, but the MC simulation yields a smaller fraction of three-track events than observed for the data. This difference is $(3.0 \pm 0.3 \pm 2.0)\%$, where the systematic error is estimated from the slight difference in the mass dependence seen in Fig. 3(b), from the uncertainties in background subtraction and from a slight difference in angular dependence. This uncertainty increases to about 10% for the mass region below 1 GeV/c^2 . The systematic difference is used to correct the observed signal size for the difference in net track-finding efficiency between that obtained from MC simulation and that observed in the experiment.

D. Detection efficiency from simulation

The selection procedures applied to the data are also applied to the MC-simulated event sample. The resulting four-pion invariant-mass distribution is shown in Fig. 4(a) for the signal and control (shaded histogram) regions. There is good qualitative agreement with the mass distribution of Fig. 2, except that no attempt was made to simulate the J/ψ and $\psi(2S)$ signals observed in the data. The mass dependence of the detection efficiency is obtained by dividing the number of reconstructed MC events in each 25 MeV/c^2 mass interval by the number generated in this same interval. The result is shown in Fig. 4(b); the curve is obtained from a polynomial fit to the distribution. The efficiency increases from 20% at

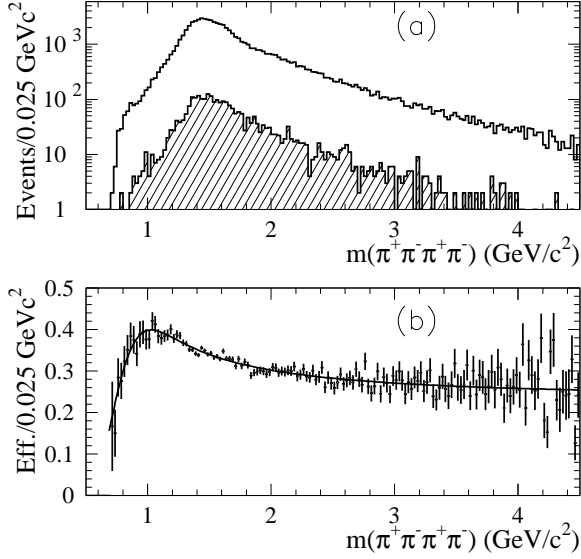


FIG. 4: (a) The four-pion mass distribution from MC simulation for the signal and control (shaded) regions of Fig. 1. (b) The mass dependence of the net reconstruction and selection efficiency obtained from simulation.

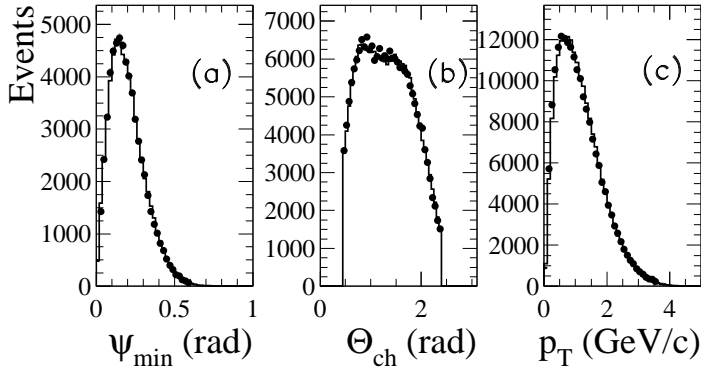


FIG. 5: (a) The distribution in track-pair opening angle for the minimum of the six values possible for each event; (b) the distribution in polar angle, and (c) the transverse momentum distribution for all pions from all events. All quantities are in the laboratory frame; the points are for data and the histograms are obtained from MC simulation.

about $0.8 \text{ GeV}/c^2$ to a maximum of 40% near $1 \text{ GeV}/c^2$, and thereafter falls off gradually with increasing mass to about 26% at $4.5 \text{ GeV}/c^2$. This efficiency estimate takes into account the geometrical acceptance of the detector for the final-state photon and the charged pions, the inefficiency of the several detector subsystems and event-loss due to additional soft-photon emission from the initial and final states.

As mentioned in Sec. II, the model used in the MC simulation assumes that the four-pion final state results predominantly from the $a_1(1260)\pi$ quasi-two-body production process [10]. A contribution from $f_0(1370)\rho(770)$ is incorporated also. In general, this model describes well

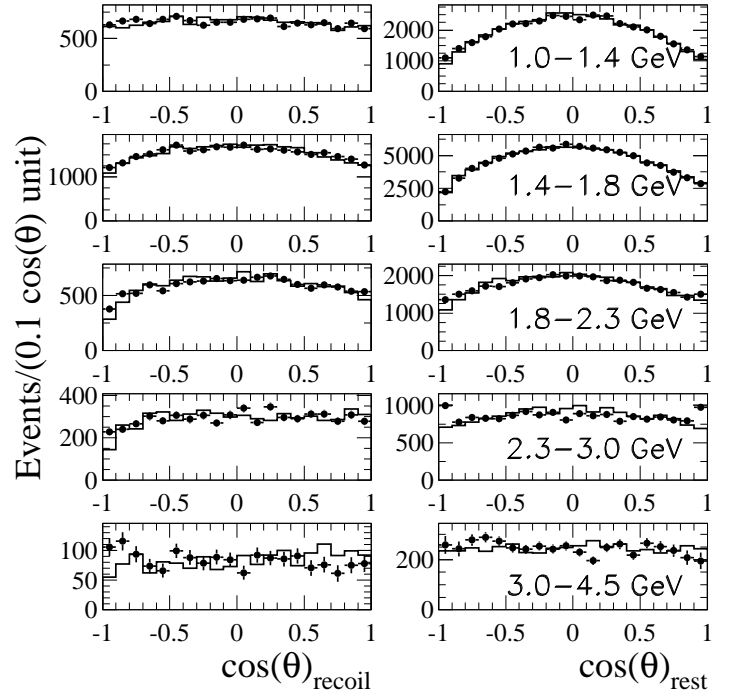


FIG. 6: The angular distribution of the lowest-momentum pion (left) and of the three most energetic pions (right) in the four-pion rest frame with respect to the direction of the four-pion system in the laboratory frame for the five regions of four-pion mass indicated. The points are data, and the histograms are MC simulation.

the distributions in many of the kinematic variables characterizing the four-pion final state. Some examples are shown in Figs. 5 and 6, in which the points with error bars represent data while the histograms are obtained from MC simulation; for both figures, the J/ψ and $\psi(2S)$ regions have been excluded. Figure 5(a) shows the distribution in ψ_{\min} , the minimum charged-pion-pair opening angle for each event, while Fig. 5(b) and Fig. 5(c) represent the distribution in polar angle, θ_{ch} , and transverse momentum, p_T , respectively, for all final-state pions. All quantities are calculated in the laboratory frame, and the overall agreement between MC simulation and data is very good. Figure 6 compares the distributions in $\cos \theta$, where θ is the angle between a charged pion in the four-pion rest frame, and the direction of the four-pion system in the laboratory frame. The distributions are presented for the five regions of four-pion mass indicated (mass increasing from top to bottom); the left column is for the lowest-momentum pion in the four-pion rest frame, and the right column sums the distributions for the others. Data and MC are in relatively good agreement up to about $2 \text{ GeV}/c^2$, but but above this value some small discrepancies appear.

In the four-pion rest frame, the angular acceptance is rather uniform. Changes in the $a_1(1260)$ and $f_0(1370)$ resonance parameter values within the ranges of their

uncertainties produce little effect. However, simulation without resonances using only four-pion phase space does produce discernible deviations from the observed angular distributions, and changes the overall acceptance by about 2%. This value is taken as an estimate of systematic uncertainty in the acceptance associated with the simulation model used.

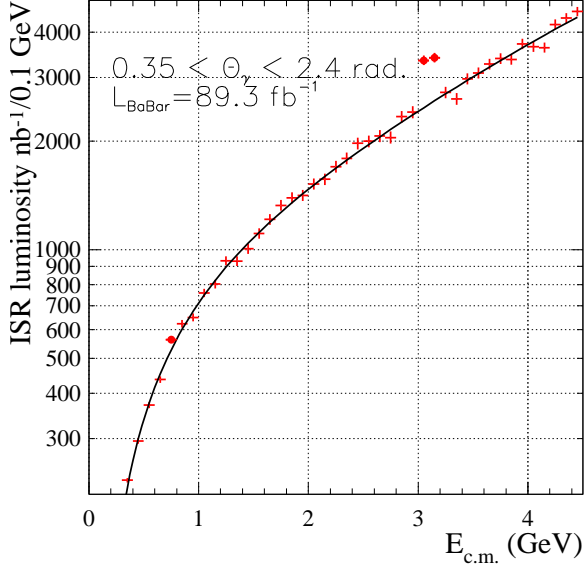


FIG. 7: The integrated ISR luminosity per 0.1 GeV in effective c.m. energy obtained from $e^+e^- \rightarrow \mu^+\mu^-\gamma$ events. The curve represents the fit used in the luminosity calculations. The point at the $\rho(770)$ mass position was excluded from the fit because of pion misidentification feed-through from the $\pi^+\pi^-\gamma$ final state. The points at the J/ψ mass position were also excluded because of ISR production of J/ψ followed by decay to $\mu^+\mu^-$.

E. Cross section for $e^+e^- \rightarrow \pi^+\pi^-\pi^+\pi^-$

Data from the reaction $e^+e^- \rightarrow \mu^+\mu^-\gamma$ are used to convert the invariant-mass distribution for an ISR-produced hadronic final state to the energy dependence of the corresponding e^+e^- cross section. The invariant mass of the muon pair $m_{\text{inv}}^{\mu\mu}$ defines an effective e^+e^- c.m. collision energy, $E_{\text{c.m.}}$. The differential luminosity, $d\mathcal{L}$, associated with the interval $dE_{\text{c.m.}}$ centered at effective collision energy $E_{\text{c.m.}}$ is then obtained from

$$d\mathcal{L}(E_{\text{c.m.}}) = \frac{dN_{\mu\mu\gamma}(E_{\text{c.m.}})}{\epsilon_{\mu\mu} \cdot (1 + \delta_{\text{FSR}}^{\mu\mu}) \cdot \sigma_{\mu^+\mu^-}(E_{\text{c.m.}}) \cdot (1 + \delta_{\text{vac}})}, \quad (4)$$

where $E_{\text{c.m.}} = m_{\text{inv}}^{\mu\mu}$; $dN_{\mu\mu\gamma}$ is the number of muon pairs in the mass interval $dm_{\text{inv}}^{\mu\mu} = dE_{\text{c.m.}}$; $\epsilon_{\mu\mu}$ is the acceptance, corrected for muon identification and soft-photon emission; $(1 + \delta_{\text{FSR}}^{\mu\mu})$ corrects for hard photon emission from final-state muons; $\sigma_{\mu^+\mu^-}(E_{\text{c.m.}})$ is the $e^+e^- \rightarrow \mu^+\mu^-$ Born cross section at center-of-mass energy $E_{\text{c.m.}}$; and $(1 + \delta_{\text{vac}})$ is the corresponding vacuum

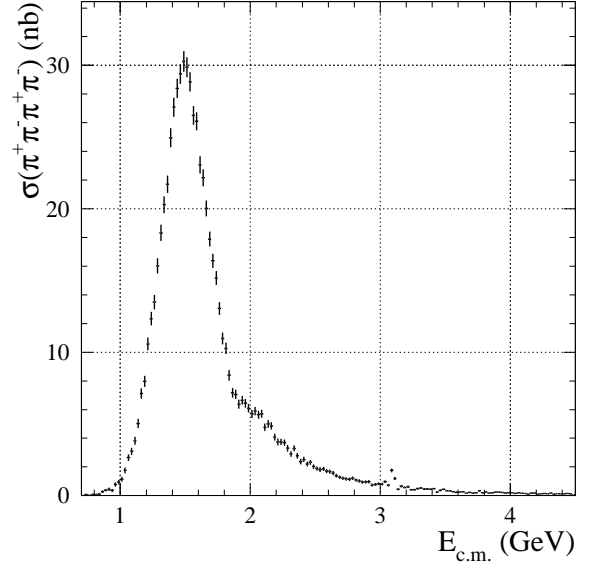


FIG. 8: The e^+e^- c.m. energy dependence of the $\pi^+\pi^-\pi^+\pi^-$ cross section measured with ISR data. The events due to $\psi(2S) \rightarrow \pi^+\pi^-J/\psi$ with $J/\psi \rightarrow \mu^+\mu^-$ (see Fig. 2) have been removed. Only statistical errors are shown.

polarization correction [20]. For the $\mu^+\mu^-\gamma$ sample obtained from a *BABAR* integrated luminosity of 89 fb^{-1} , the dependence of the resulting differential luminosity on $E_{\text{c.m.}}$ is shown in Fig. 7 in units of $[\text{nb}^{-1}/0.1 \text{ GeV}]$. From a detailed study of the $e^+e^- \rightarrow \mu^+\mu^-\gamma$ detection and identification efficiency described in detail in Ref. [7] and comparison of the observed invariant-mass spectrum with theoretical calculations, we estimate the systematic uncertainty associated with luminosity determination to be 3%.

The four-pion e^+e^- cross section can then be calculated from

$$\sigma(\pi^+\pi^-\pi^+\pi^-)(E_{\text{c.m.}}) = \frac{dN_{4\pi\gamma}(E_{\text{c.m.}}^{\pi})}{d\mathcal{L}(E_{\text{c.m.}}) \cdot \epsilon_{4\pi}^{\text{corr}} \cdot \epsilon_{4\pi}^{\text{MC}}(E_{\text{c.m.}}^{\pi})}, \quad (5)$$

where $E_{\text{c.m.}}^{\pi} \equiv m_{\text{inv}}^{\mu\mu} \equiv E_{\text{c.m.}}^{\pi} \equiv m_{\text{inv}}^{4\pi} \equiv E_{\text{c.m.}}$ with $m_{\text{inv}}^{4\pi}$ the invariant mass of the four-charged-pion system; $dN_{4\pi\gamma}$ is the number of selected four-pion events after background subtraction in the interval $dE_{\text{c.m.}}$ and $\epsilon_{4\pi}^{\text{MC}}(E_{\text{c.m.}})$ is the corresponding detection efficiency obtained from the MC simulation. The factor $\epsilon_{4\pi}^{\text{corr}}$ takes into account the difference between the χ^2 distributions for data and MC events, and the tracking-efficiency discrepancies discussed in Sec. IV B and Sec. IV C respectively.

Since the four-pion cross section calculation involves the ratio of the numbers of observed $4\pi\gamma$ and $\mu\mu\gamma$ events, corrections related to multi-soft-photon emission in the initial state and to the detection efficiency of the ISR photon cancel, these being the same for both reactions. Also, since $d\mathcal{L}$ has been corrected for vacuum polarization and final-state soft-photon emission, the four-pion cross section measured in this way includes effects due to

vacuum polarization and final-state soft-photon emission.

We studied the resolution in four-pion mass with MC simulation and found that the r.m.s. deviation varied from 6.2 MeV/ c^2 at mass 1.5 GeV/ c^2 to 7.5 MeV/ c^2 at 3 GeV/ c^2 . Since the cross section has no sharp peaks (J/ψ region is discussed below) and the measurements are presented in mass intervals of 25 MeV/ c^2 , the resolution has negligible effect on the measured energy dependence.

The energy dependence of the cross section for the reaction $e^+e^- \rightarrow \pi^+\pi^-\pi^+\pi^-$ after all corrections is shown in Fig. 8. It reaches a peak value of about 30 nb near 1.5 GeV, with a shoulder at 1.9–2.1 GeV, followed by a monotonic decrease toward higher energies perturbed only by a small peak at the J/ψ mass position. The events due to $\psi(2S) \rightarrow \pi^+\pi^-J/\psi$ with $J/\psi \rightarrow \mu^+\mu^-$, seen in Fig. 2, have been removed. The luminosity, number of events, and corrected cross section for each 25 MeV interval are presented in Table III. For $g-2$ calculations, vacuum polarization contributions should be excluded. Suitably modified cross section values are presented in the last column of Table III.

We checked the stability of the measured cross section by comparing the results obtained under conditions of different DCH voltage, which affects track-finding efficiency, and results obtained from data taken at the $\Upsilon(4S)$ mass and below the $B\bar{B}$ threshold. No significant discrepancies were observed.

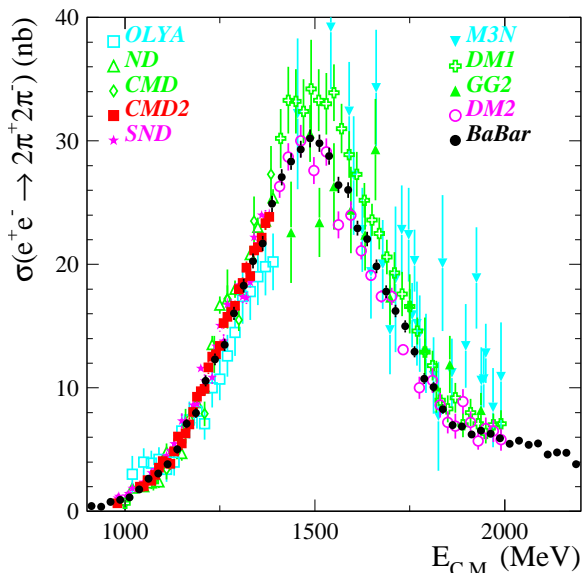


FIG. 9: The energy dependence of the $e^+e^- \rightarrow \pi^+\pi^-\pi^+\pi^-$ cross section obtained with *BABAR* ISR data (black points) in comparison with that from direct e^+e^- production measurements. Only statistical errors are shown.

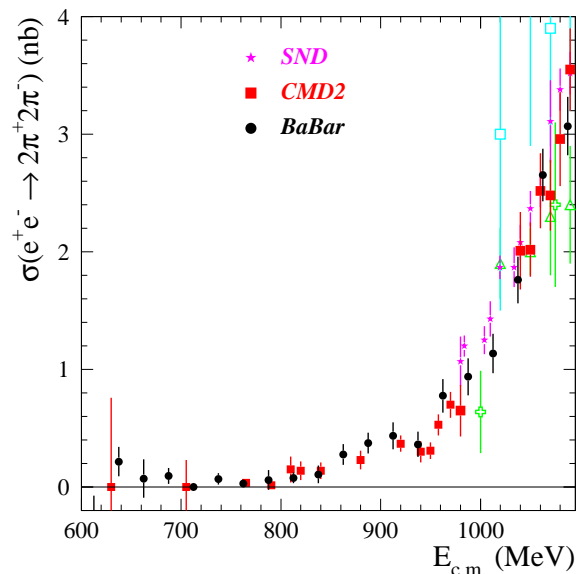


FIG. 10: A detailed view of the energy dependence of the $e^+e^- \rightarrow \pi^+\pi^-\pi^+\pi^-$ cross section near threshold; All experimental points are indicated as in Fig. 9. Only statistical errors are shown.

F. Summary of systematic studies

The measured four-pion cross section values shown in Fig. 8 and summarized in Table III include only statistical errors. The systematic errors discussed in previous sections are summarized in Table I, along with the corrections that were applied to the measurements.

The two systematic corrections applied to the measured cross sections sum up to +6% with half of this value taken as a systematic uncertainty. The systematic errors that cancel in the ratio to $\mu\mu\gamma$ are the photon detection efficiency and the ISR soft-photon radiative correction uncertainty.

G. Physics results

The four-charged-pion cross section measured by *BABAR* can be compared with existing e^+e^- measurements only up to 2.0 GeV—the maximum c.m. energy up to which measurements of this channel have been published. Figures 9 and 10 show the cross section in comparison with all existing e^+e^- data for c.m. energies in the 0.7–2.2 GeV range.

The measured cross section is in good agreement with the precision data taken at VEPP-2M by SND [21] and CMD-2 [18, 22] in the energy range 0.7–1.4 GeV, as well as with data obtained at DCI by DM2 [23] in 1.4–2.0 GeV range. The systematic errors for *BABAR* data are comparable to, or smaller than, those for these experiments.

Different mass combinations were studied in data and MC events to search for any structures or states not included in the simulation. Figure 11 shows the scatter-

TABLE I: Summary of systematic errors for $e^+e^- \rightarrow \pi^+\pi^-\pi^+\pi^-$ cross section

Source	Correction applied	Systematic error
Luminosity from $\mu\mu\gamma$	-	3%
MC-data difference in $\chi^2 < 30$ requirement	+3%	5% for $m_{4\pi} < 1.0$ GeV/ c^2
Background subtraction	-	2%
		1%
		10% for $m_{4\pi} < 1.0$ GeV/ c^2
		3% for $m_{4\pi} > 3.0$ GeV/ c^2
MC-data difference in track losses	+3%	2%
Radiative corrections accuracy	-	1%
Acceptance from MC (model-dependent)	-	2% for < 3 GeV
		15% for the rest
Total	+6%	12% for $m_{4\pi} < 1.0$ GeV/ c^2
(assuming no correlations)		5% for $1.0 < m_{4\pi} < 3.0$ GeV/ c^2
		16% for $m_{4\pi} > 3.0$ GeV/ c^2

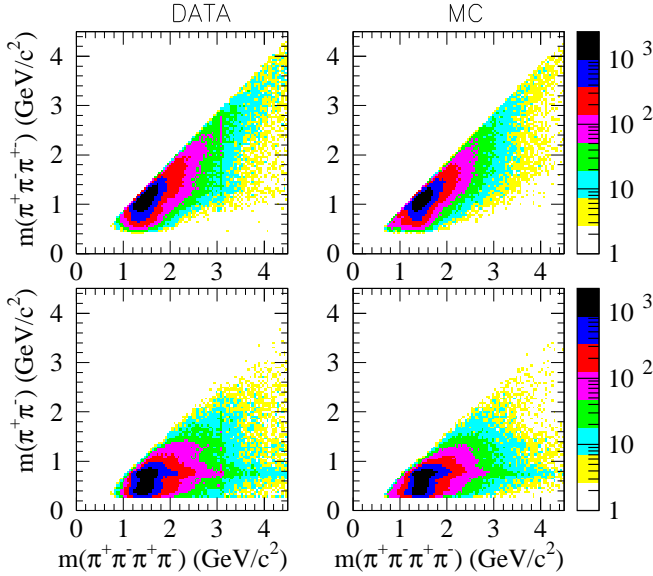


FIG. 11: The two-pion (bottom) and three-pion (top) vs. four-pion invariant mass distributions for data (left) and simulation (right); signals corresponding to J/ψ and $\psi(2S)$ production are present in the data, but are not included in the simulation. Otherwise, agreement between data and MC simulation is quite good.

plots of 3π - and 2π -mass versus 4π -mass for data and MC events. Good agreement is seen except for narrow regions around the J/ψ and $\psi(2S)$ masses, which are not included in the simulation.

In order to make a more detailed study, five intervals of 4π -mass are selected: (1) 1.0–1.4 GeV/ c^2 (for comparison with CMD-2), (2) 1.4–1.8 GeV/ c^2 (peak in cross section, see Fig. 8), (3) 1.8–2.3 GeV/ c^2 (shoulder), (4) 2.3–3.0 GeV/ c^2 , and (5) 3.0–4.5 GeV/ c^2 (narrow regions around the J/ψ and $\psi(2S)$ are excluded). Figure 12 shows the one-dimensional projections of Fig. 11 of the 2π - and 3π -mass for the above five regions for data and

MC events. In these distributions we subtract the background using control samples in the χ^2 distributions from data and JETSET simulation, as described above.

There is excellent agreement between data and MC events in the 1.0–1.4 GeV/ c^2 region where $a_1(1260)$ production is severely limited by the available phase space, and $f_0(1370)$ production is almost entirely excluded. Discrepancies begin to appear in the higher mass regions, and in particular a relatively narrow bump in the $\pi^+\pi^-$ combinations at about 1.3 GeV/ c^2 for the 2.3–3.0 GeV/ c^2 region is not reproduced by the simulation. The world averages reported by the Particle Data Group (PDG) [17] for the $a_1(1260)$ mass and width are not well-determined; in the simulation we use 1.33 GeV/ c^2 and 0.57 GeV respectively. These values were obtained from a combined analysis of CLEO and CMD-2 data [19].

The 3π -mass data of Fig. 12 (1.8–2.3 GeV/ c^2) seem to favor a lower $a_1(1260)$ mass value than the 1.33 GeV/ c^2 used in simulating the $a_1(1260)$. In the simulation, the $f_0(1370)$ mass and width were set to 1.3 GeV/ c^2 and 0.6 GeV respectively. The 2π -mass data for the 2.3–3.0 GeV/ c^2 region seem to indicate the need for a significantly smaller width, although the peak around 1.3 GeV/ c^2 may also be due to significantly higher production of $f_2(1270)$ than in the present model.

In Fig. 12, the right-hand column of plots corresponds to the highest di-pion mass value when one other di-pion mass is within 25 MeV/ c^2 of the ρ mass. The flat, broad band below 1 GeV/ c^2 is the reflection of the ρ band in $a_1(1260)$ decay. The comparatively narrow peak around 1.3 GeV/ c^2 in the 2.3–3.0 GeV/ c^2 region indicates the need for $f_0(1370)\rho$ in the simulation.

A full partial wave analysis is required in order to arrive at a more precise interpretation of the data. However, this requires a simultaneous analysis of the $\pi^+\pi^-\pi^0\pi^0$ final state, which is beyond the scope of this study.

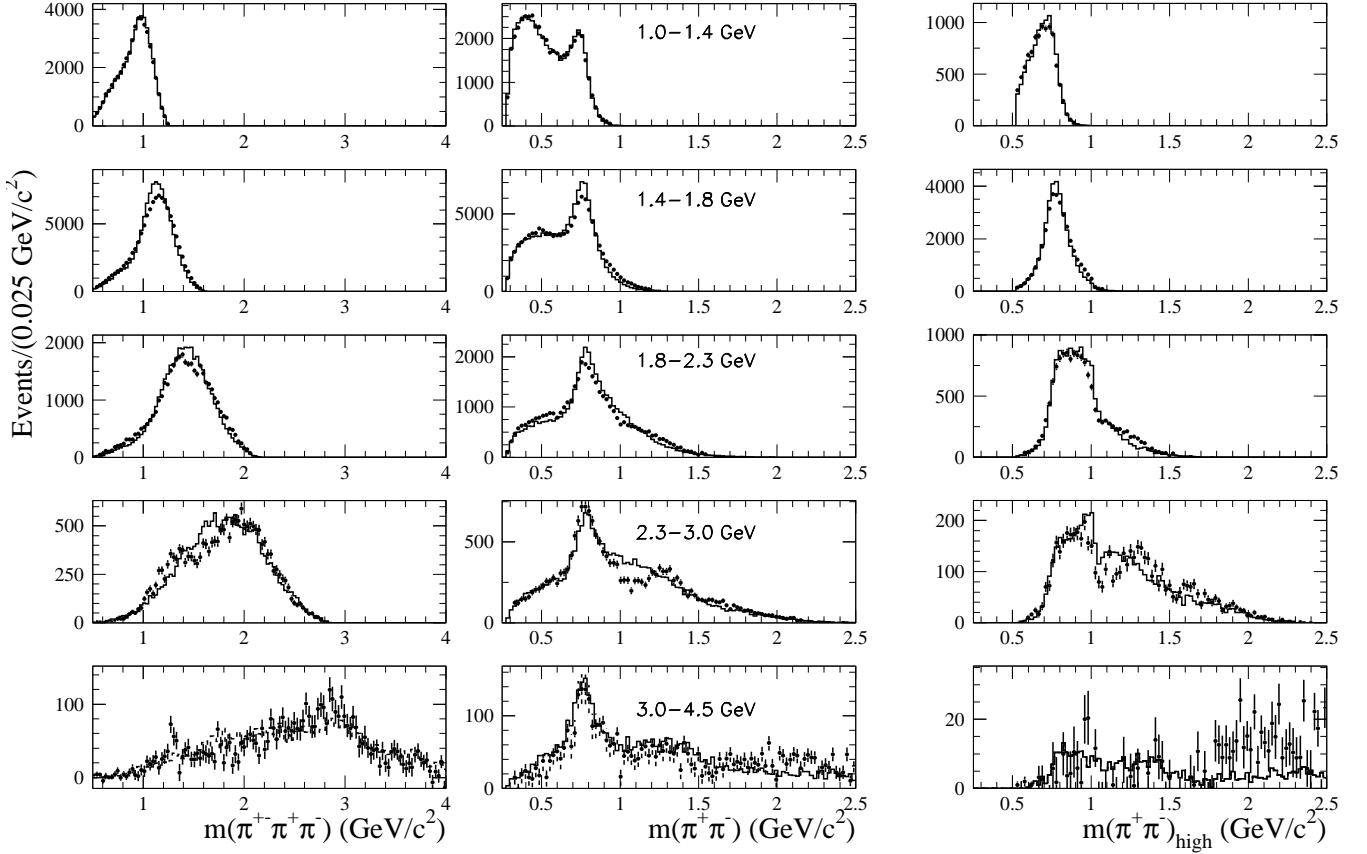


FIG. 12: The three-pion (left) and $\pi^+\pi^-$ (center) mass distributions; the points represent data, the histograms simulation, and there are four entries per event. Five regions of four-pion mass are indicated in the center plots. For events having a $\pi^+\pi^-$ mass combination in the $\rho(770)$ region, the distribution of the highest mass other $\pi^+\pi^-$ pair is shown in the plots to the right.

V. THE $K^+K^-\pi^+\pi^-$ FINAL STATE

The constrained fit of the four-charged-track events to the hypothesis of two oppositely charged kaons and two charged pions, where at least one of the kaons has positive particle identification, allows us to select this final state. Figure 13 shows the χ^2 distributions for both data and simulation, where the simulation of the $K^+K^-\pi^+\pi^-$ reaction uses a point-like matrix element with a cross section energy dependence close to that which we observe experimentally, and all radiative processes are included. Also shown is the estimated contribution from the 4π final state arising from particle misidentification, as obtained from simulation.

Figure 14(a) presents the simulated mass distribution for the $2K2\pi$ events; the mass dependence of the efficiency, calculated as a ratio of selected to generated $2K2\pi$ MC events, is shown in Fig. 14(b).

The selections $\chi^2_{2K2\pi} < 20$, $\chi^2_{4\pi} > 30$ and $\chi^2_{4K} > 20$ are used, leaving a negligible number of $4K$ and 0.5% of 4π events (from simulation) in the final sample. The background subtraction procedure which uses the control sample with $20 < \chi^2_{2K2\pi} < 40$ is applied. The background from 4π events is not subtracted by this proce-

dure, and 0.5% of the events shown in Fig. 2 are used to make an additional correction.

In Fig. 15 we show the $K^+K^-\pi^+\pi^-$ invariant mass distribution for the events that passed the selection procedure. The points with error bars show the background distribution from the control sample with $20 < \chi^2_{2K2\pi} < 40$ and the shaded histogram is the expected non-ISR background from JETSET MC simulation. Both are used for background subtraction. A very clear J/ψ signal is seen.

Using the number of observed events, efficiency, and ISR luminosity, we obtain the $e^+e^- \rightarrow K^+K^-\pi^+\pi^-$ cross section shown in Fig. 16, which also displays the DM1 data [25]. Table IV presents the cross section in 25 MeV bins, together with the “undressed” (no vacuum polarization) cross section. The systematic errors are dominated by uncertainty in the acceptance simulation (10%) and the difference between the kaon identification efficiencies for data and MC events (up to 5% per track), and are estimated to be 15%.

Figure 17 shows the $K\pi$ mass combinations. Production of $K\pi$ pairs is dominated by the $K^{*0}(892)$ clearly seen in Fig. 17(a). There also appears to be evidence of $K_2^*(1430)$ production in the $2K2\pi$ sample seen in the pro-

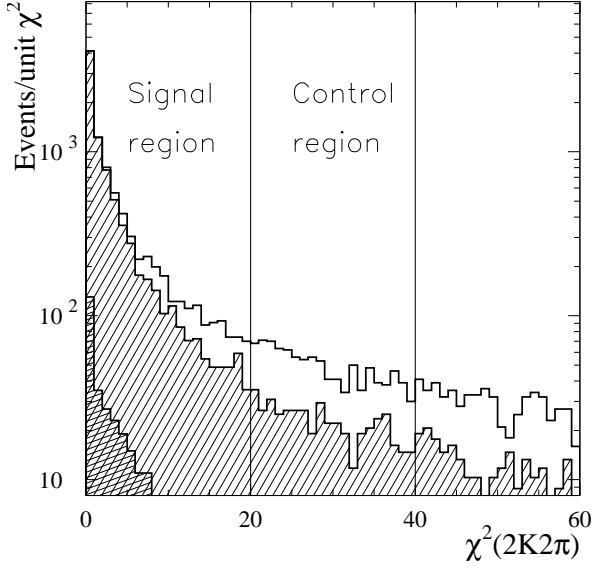


FIG. 13: The one-constraint χ^2 distributions for the four-charged-track data events and $K^+K^-\pi^+\pi^-$ Monte Carlo events (shaded histogram) fitted to the $K^+K^-\pi^+\pi^-$ hypothesis. At least one kaon must be identified. The cross-hatched histogram is the estimated background contribution from four-charged-pion ISR events. The signal and control regions are indicated.

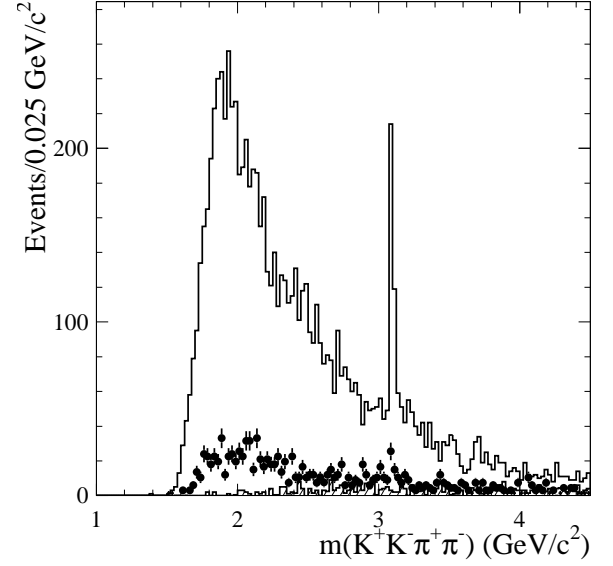


FIG. 15: The $K^+K^-\pi^+\pi^-$ invariant mass distribution for the signal region of Fig. 13. The points indicate the background estimated from the difference between data and MC simulation for the control region of Fig. 13 normalized to the difference between the number of data and MC events in the signal region of Fig. 13. The shaded histogram corresponds to the non-ISR background estimated using JETSET.

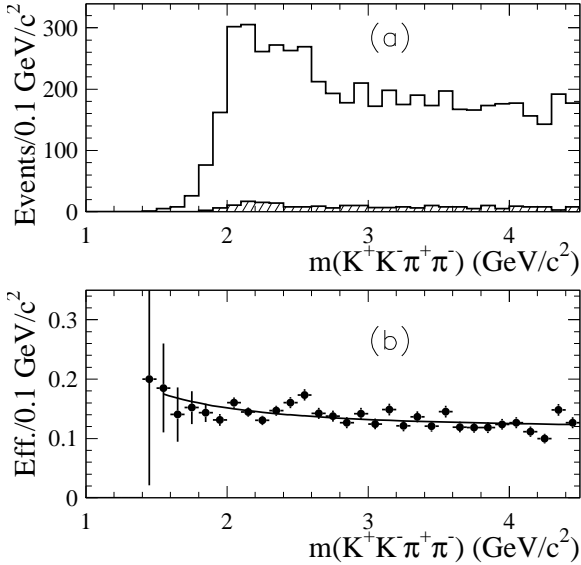


FIG. 14: (a) The $K^+K^-\pi^+\pi^-$ mass distribution from simulation for the signal and control (shaded) regions of Fig.13; (b) the mass dependence of the net reconstruction and selection efficiency obtained from simulation.

jection plot of Fig. 17(a) shown in Fig. 17(c). No structures in $m(K^+\pi^+)$ or in $m(K^-\pi^-)$ are seen in Fig. 17(b). The $K\pi$ mass distribution for the other $K\pi$ combination for events in the $K^{*0}(892)$ bands of Fig. 17(a) is shown in Fig. 17(d); events in the overlap region of the two bands are included only once to avoid double-counting. The ab-

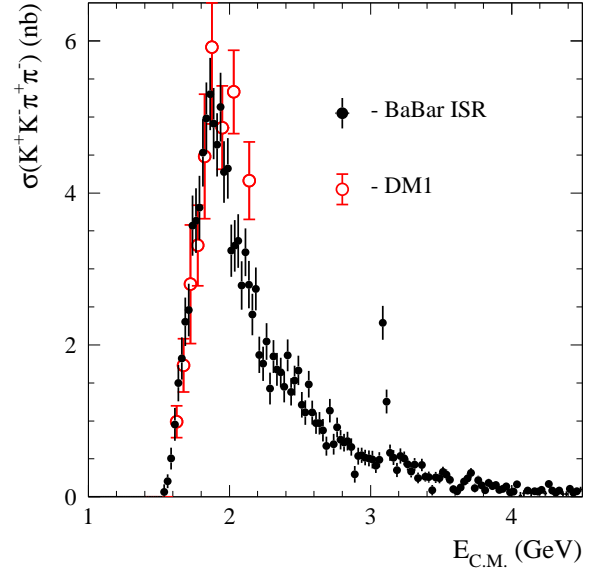


FIG. 16: The c.m. energy dependence of the $e^+e^- \rightarrow K^+K^-\pi^+\pi^-$ cross section obtained from ISR events at BABAR compared with the only direct e^+e^- measurement, by DM1. Only statistical errors are shown.

sence of a clear $K^{*0}(892)$ or $K_2^{*0}(1430)$ signal in Fig. 17(d) indicates that $K^{*0}(892)\bar{K}^{*0}(892)$ and $K^{*0}(892)K_2^{*0}(1430)$ quasi-two-body production reactions are small.

When events in the $K^{*0}(892)$ bands of Fig. 17(a) are removed, the scatter-plot $m(\pi^+\pi^-)$ vs. $m(K^+K^-)$ in Fig. 18(a) shows the presence of the ρ^0 and ϕ resonances.

The $\pi^+\pi^-$ (Fig. 18(b)) and K^+K^- (Fig. 18(c)) mass projections from Fig. 18(a) exhibit clear ρ^0 and ϕ signals, respectively. Figure 18(d) shows the $\pi^+\pi^-$ mass distribution for events with $m(K^+K^-)$ in the ϕ region. The absence of any ρ signal is consistent with C conservation; there might be slight evidence of $f_0(980)$ production.

The three-body mass combinations are also of potential interest. We consider these in two categories. For the first category, we require that there be a $K^\mp\pi^\pm$ combination in one of the $K^{*0}(892)$ bands of Fig. 17(a). The $K^{*0}(892)K^\pm$ invariant mass behavior for such events is shown in Figs. 19(a,b). In Fig. 19(b), there is a strong peak just below 1.5 GeV/ c^2 followed by a shoulder around 1.6–1.7 GeV/ c^2 and a rapid drop in the 1.8–2.0 GeV/ c^2 region. The peak could correspond to a presently unknown isovector state decaying to $K^{*0}\bar{K} + \bar{K}^{*0}K$. The corresponding $K^{*0}\pi$ behavior is shown in Figs. 19(c,d). The mass projection in Fig. 19(c) shows a broad structure in the region of the $K_1(1270)$ and $K_1(1410)$, both of which are known to decay through $K^{*0}\pi$. The scatter-plot of $m(K^{*0}\pi)$ vs. $m(K^{*0}K)$ in Fig. 19(d) shows that the low-mass enhancements of Figs. 19(b,c) are highly-correlated.

For the second category, we exclude events with at least one $K\pi$ combination in a $K^{*0}(892)$ band of Fig. 17(a). As shown in Fig. 18(c), a subset of the remaining events contains a ϕ signal. When the events in the ϕ region are combined with the remaining π^\pm , the $\phi\pi^\pm$ mass distribution of Fig. 20(a) is obtained. This shows a peak in the mass region 1.25–1.4 GeV/ c^2 , followed by a second broad bump in the 1.5–1.8 GeV/ c^2 region. If the ϕ region is excluded, the rather featureless mass distribution of Fig. 20(b) is obtained. However, the scatter-plot of $m(\pi^+\pi^-)$ vs. $m(K^\pm\pi^+\pi^-)$ in Fig. 20(c) for these events shows clear evidence for ρ production correlated with $K^\pm\pi^+\pi^-$ mass in the 1.2–1.5 GeV/ c^2 region. The $K_1(1270)$ couples quite strongly to $K\rho$ [17], and so may be produced in this final state. However, the $K_1(1410)$ is almost decoupled from $K\rho$ [17], and so cannot be the source of the events in the 1.4–1.5 GeV/ c^2 region.

There is evidence in the $K^+K^-\pi^+\pi^-$ final state for several interesting, but complex, structures. Detailed understanding will require data on $K^+K^-\pi^0\pi^0$ and also on four-body final states involving neutral kaons.

VI. THE $K^+K^-K^+K^-$ FINAL STATE

The one-constraint fit for the four-charged-kaon hypothesis with $\chi^2_{4K} < 20$ selection gives a very pure sample of this final state. The main background contribution is from the reaction with two charged kaons and two misidentified charged pions. We reduced this background greatly by adding to the initial selection criterion the requirements that three or four of the charged particles have good kaon identification and that $\chi^2_{2K2\pi} > 20$ for the fit to the reaction with two kaons and two pions. Background from the 4π final state is negligible.

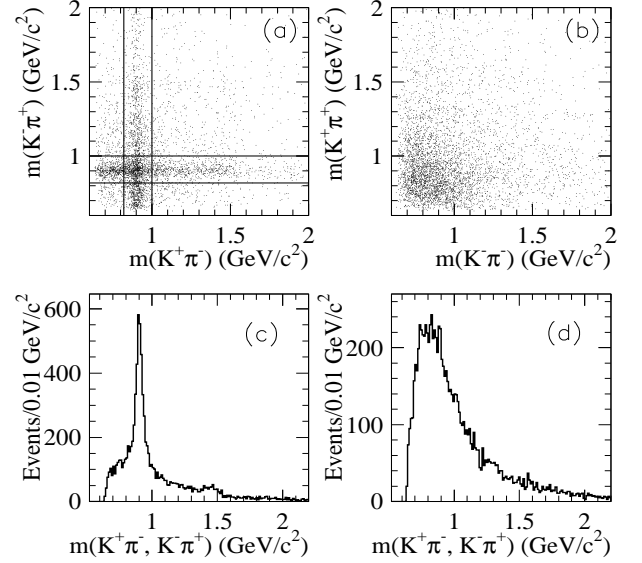


FIG. 17: For the $K^+K^-\pi^+\pi^-$ data sample: (a) the scatter-plot of the $K^+\pi^-$ and $K^-\pi^+$ invariant mass values; (b) the scatter-plot of the $K^+\pi^+$ and $K^-\pi^-$ invariant mass values; (c) the $K^+\pi^-$ or $K^-\pi^+$ mass projection of (a); (d) the mass distribution for other $K\pi$ combinations for events in the $K^{*0}(892)$ bands of (a).

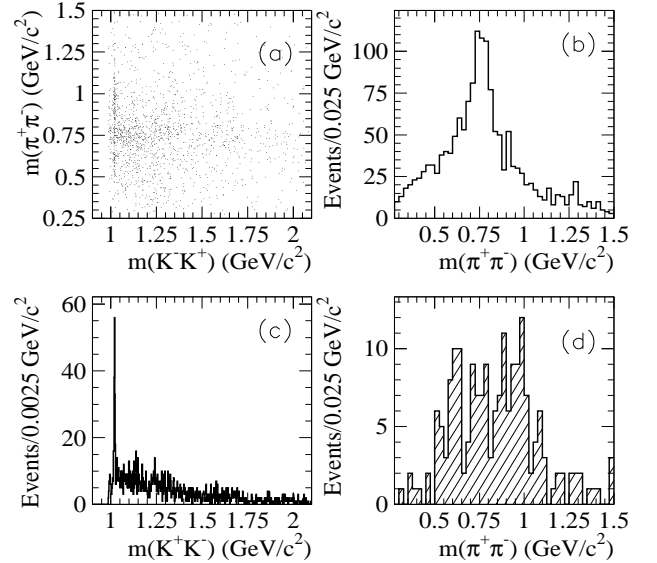


FIG. 18: For the $K^+K^-\pi^+\pi^-$ data sample, after removing events contributing to the $K^{*0}(892)$ mass regions indicated in Fig. 17(a): (a) the scatter-plot of $\pi^+\pi^-$ and K^+K^- mass values; (b) the $\pi^+\pi^-$ mass projection of (a); (c) the K^+K^- mass projection of (a); (d) the $\pi^+\pi^-$ mass projection of (a) for events in the $\phi(1020)$ mass peak.

Figure 21 shows the χ^2 distributions for data and simulation. The simulation of the $4K$ final state uses a point-like matrix element with cross section behavior close to what we observe experimentally, and with all radiative processes included. Also shown is the contribution from the $2K2\pi$ final state obtained from the simulation (cross-

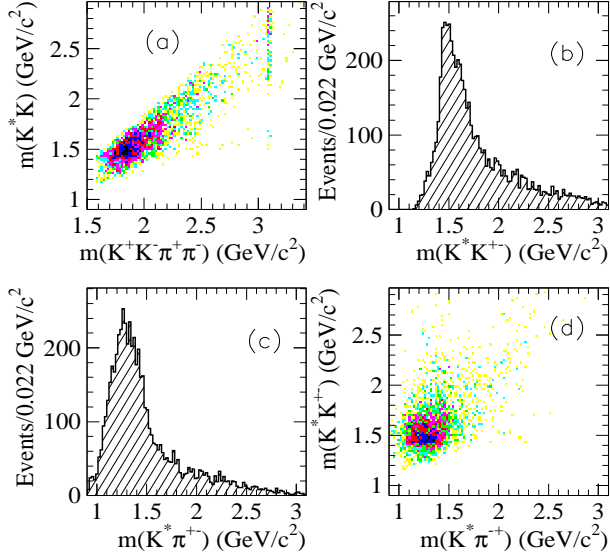


FIG. 19: The $2K2\pi$ events from the $K^{*0}(892)$ bands in Fig. 17(a): (a) the $K^{*0}(892)K^\pm$ vs. $K^+K^-\pi^+\pi^-$ invariant mass distribution scatter-plot; (b) the $K^{*0}(892)K^\pm$ mass projection; (c) the $K^{*0}(892)\pi^\pm$ mass distribution; (d) the $m(K^{*0}\pi^\pm)$ vs. $m(K^{*0}K^\pm)$ scatter-plot.

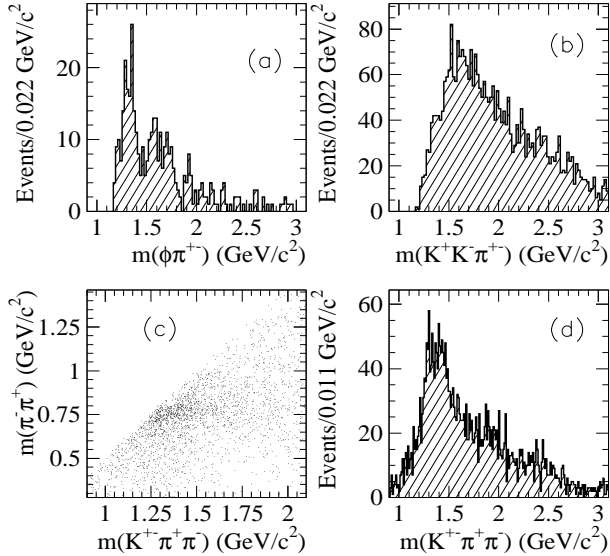


FIG. 20: The $2K2\pi$ events with the $K^{*0}(892)$ bands in Fig. 17(a) excluded: (a) the $K^+K^-\pi^\pm$ mass distribution with the K^+K^- mass in the ϕ region; (b) the $K^+K^-\pi^\pm$ mass distribution with K^+K^- in the ϕ mass region excluded; (c) the $\pi^+\pi^-$ vs. $K^\pm\pi^+\pi^-$ scatter-plot, and (d) the $K^\pm\pi^+\pi^-$ projection, for the events from (b).

hatched).

Figure 22(a) shows the simulated mass distribution for $4K$ events, and Fig. 22(b) presents the detection efficiency calculated as the ratio of selected to generated $4K$ MC events.

In Fig. 23 the $K^+K^-K^+K^-$ invariant mass distribution is shown for the data in the signal region, and also for

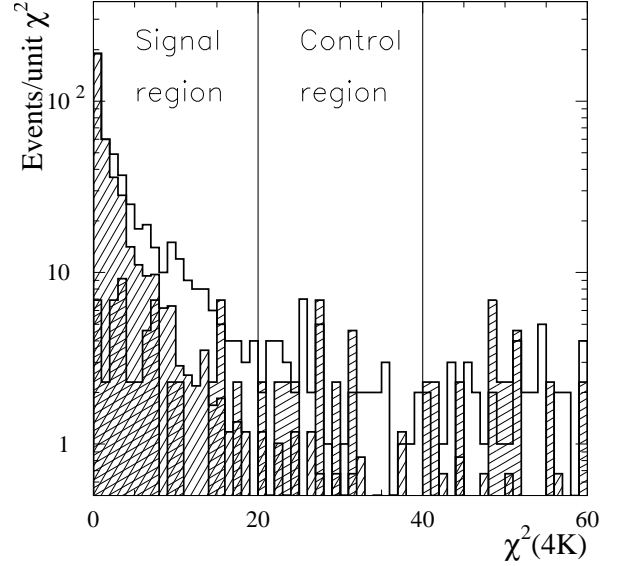


FIG. 21: The one-constraint χ^2 distributions for four-charged-track data events and $K^+K^-K^+K^-$ Monte Carlo events (shaded histogram) fitted to the $K^+K^-K^+K^-$ hypothesis. At least three kaons must be identified. The cross-hatched histogram is the estimated background contribution from $K^+K^-\pi^+\pi^-$ ISR events. The signal and control regions are indicated.

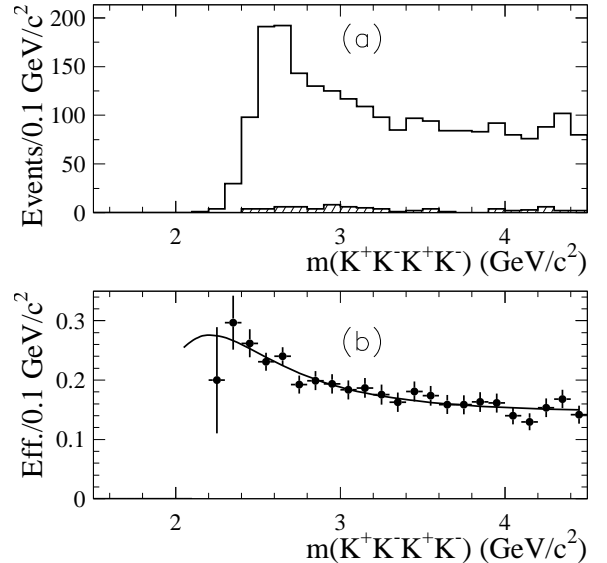


FIG. 22: (a) The $K^+K^-K^+K^-$ mass distribution from simulation for the signal and control (shaded) regions of Fig. 21; (b) the mass dependence of the net reconstruction and selection efficiency obtained from simulation.

background estimated from the $20 < \chi_{4K}^2 < 40$ control sample (points). The shaded histogram shows the expected non-ISR background from the JETSET MC simulation. A clear signal due to the J/ψ is seen. The number of signal events as a function of four-kaon mass is obtained by subtracting the background contributions estimated from the control sample and from the JETSET

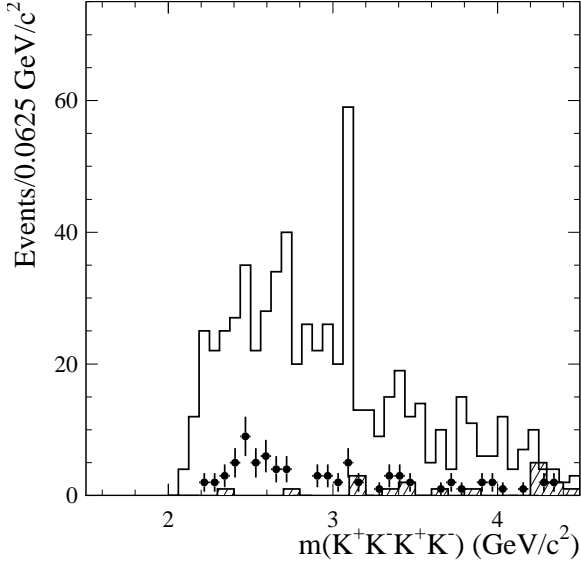


FIG. 23: The $K^+K^-K^+K^-$ invariant-mass distribution for the signal region of Fig. 21. The points indicate the background estimated from the difference between data and MC simulation for the control region of Fig. 21, normalized to the difference between the number of data and MC events in the signal region of Fig. 21. The shaded histogram corresponds to the non-ISR background estimated from JETSET.

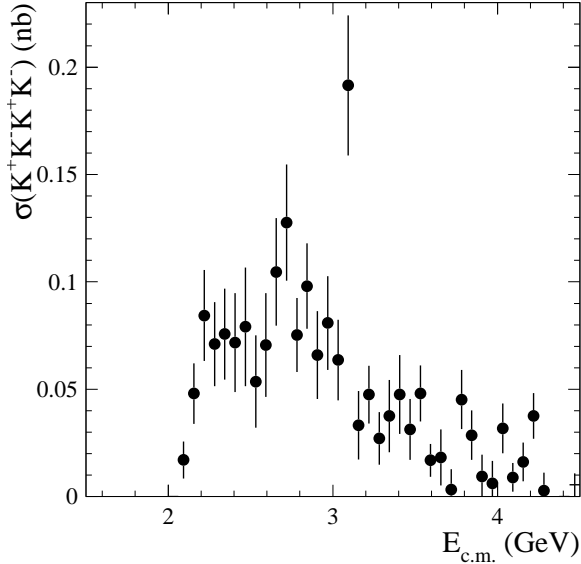


FIG. 24: The c.m. energy dependence of the $e^+e^- \rightarrow K^+K^-K^+K^-$ cross section obtained from ISR events at BABAR. Only statistical errors are shown.

MC simulation.

Using the number of four-charged-kaon events observed, the acceptance discussed previously, and the ISR luminosity, we calculate the cross section for the reaction $e^+e^- \rightarrow K^+K^-K^+K^-$. The results with statistical errors only are displayed in Fig. 24, and the values are listed in Table V. There are no published electron-positron data for comparison. Systematic errors are dominant

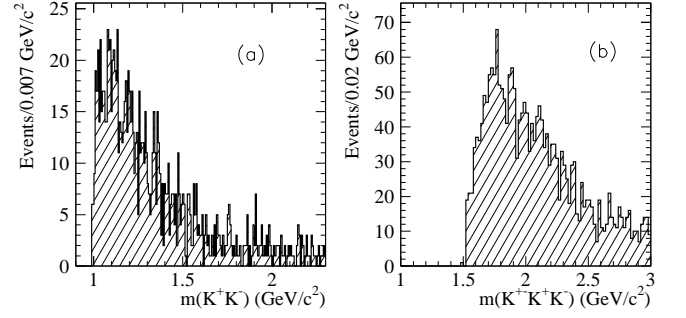


FIG. 25: (a) The K^+K^- and (b) the $K^\pm K^+K^-$ invariant mass distributions for events from the $K^+K^-K^+K^-$ sample.

for these measurements. These uncertainties are due to the absence of a detailed model for the acceptance simulation, to uncertainties in the background subtractions, and to differences in kaon identification efficiency in the MC simulation and the data. The overall estimated systematic error is about 25%. The K^+K^- and $K^\pm K^+K^-$ invariant mass distributions are shown in Fig. 25 (four entries per event). If there is any ϕ production it is small, and neither mass distribution shows evidence of significant structure.

VII. THE J/ψ REGION

Figure 26 shows an expanded view of the J/ψ mass region in Fig. 2 for the four-pion data sample. The signals from $J/\psi \rightarrow \pi^+\pi^-\pi^+\pi^-$ and $\psi(2S) \rightarrow J/\psi\pi^+\pi^- \rightarrow \mu^+\mu^-\pi^+\pi^-$ (without muon identification) are clearly seen. The observation of J/ψ decaying into four pions gives a direct measurement of the 4π -mass resolution and the absolute energy scale. A fit with a Gaussian for the J/ψ peak and a polynomial function for the continuum, gives $\sigma_{m(4\pi)} = 8 \text{ MeV}/c^2$ and less than $1 \text{ MeV}/c^2$ difference from the PDG [17] value for the J/ψ mass. The observed mass resolution agrees with the simulation within 10%.

The observed 270 ± 20 events at the J/ψ peak can be used to calculate the branching fraction for $J/\psi \rightarrow \pi^+\pi^-\pi^+\pi^-$. The simulation shows that because of radiative effects only 89% of the signal events are under the Gaussian curve. This value is in good agreement with that obtained from $\psi(2S)$ peak $87.7 \pm 1.3\%$ (see below) which is used for calculations. Using the corrected

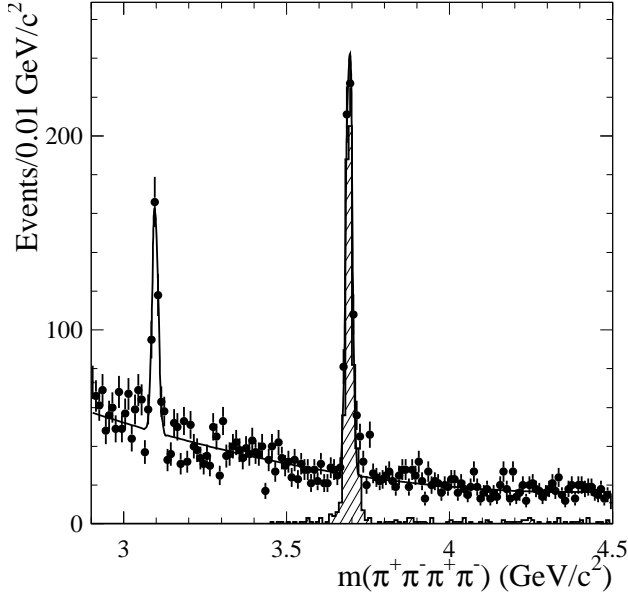


FIG. 26: The $\pi^+\pi^-\pi^+\pi^-$ mass distribution for ISR-produced $e^+e^- \rightarrow \pi^+\pi^-\pi^+\pi^-$ events in the J/ψ - $\psi(2S)$ region; there are clear signals at the J/ψ and $\psi(2S)$ mass positions. The shaded region at the latter corresponds to $\psi(2S) \rightarrow J/\psi\pi^+\pi^-$, with $J/\psi \rightarrow \mu^+\mu^-$ and the muons are treated as pions.

number, we can calculate the products:

$$\begin{aligned}
 B_{J/\psi \rightarrow 4\pi} \cdot \sigma_{\text{int}}^{J/\psi} &= \frac{N(J/\psi \rightarrow \pi^+\pi^-\pi^+\pi^-)}{d\mathcal{L}/dE \cdot \epsilon_{\text{MC}}} \\
 &= 46.8 \pm 3.5 \pm 3.3 \text{ nb MeV} , \\
 B_{J/\psi \rightarrow 4\pi} \cdot \Gamma_{ee}^{J/\psi} &= \frac{N(J/\psi \rightarrow \pi^+\pi^-\pi^+\pi^-) \cdot m_{J/\psi}^2}{6\pi^2 \cdot d\mathcal{L}/dE \cdot \epsilon_{\text{MC}} \cdot C} \\
 &= (1.95 \pm 0.14 \pm 0.13) \times 10^{-2} \text{ keV} ,
 \end{aligned}$$

where

$$\sigma_{\text{int}}^{J/\psi} = 6\pi^2 \Gamma_{ee}^{J/\psi} C / m_{J/\psi}^2 = 12790 \pm 850 \text{ nb} \cdot \text{MeV}$$

is the integral over the J/ψ excitation curve; $\Gamma_{ee}^{J/\psi}$ is the electronic width; $d\mathcal{L}/dE = 25.3 \text{ nb}^{-1}/\text{MeV}$ is the ISR luminosity at the J/ψ mass; $\epsilon_{\text{MC}} = 0.26 \pm 0.01$ is the detection efficiency from simulation with the corrections discussed in Sec. IV F; and $C = 3.894 \times 10^{11} \text{ nb MeV}^2$ is a conversion constant. The systematic error includes 3% uncertainty from the ISR luminosity, 3% from efficiency, and 5% uncertainty from background subtraction. The subscript “4 π ” for branching fractions refers to the $\pi^+\pi^-\pi^+\pi^-$ final state exclusively.

Using $\Gamma_{ee}^{J/\psi} = 5.40 \pm 0.17 \text{ keV}$ [17], we obtain the result $B_{J/\psi \rightarrow 4\pi} = (3.61 \pm 0.26 \pm 0.26) \times 10^{-3}$, substantially more precise than the current PDG value $B_{J/\psi \rightarrow 4\pi} = (4.0 \pm 1.0) \times 10^{-3}$ [17]. The systematic error includes 3% uncertainty in $\Gamma_{ee}^{J/\psi}$.

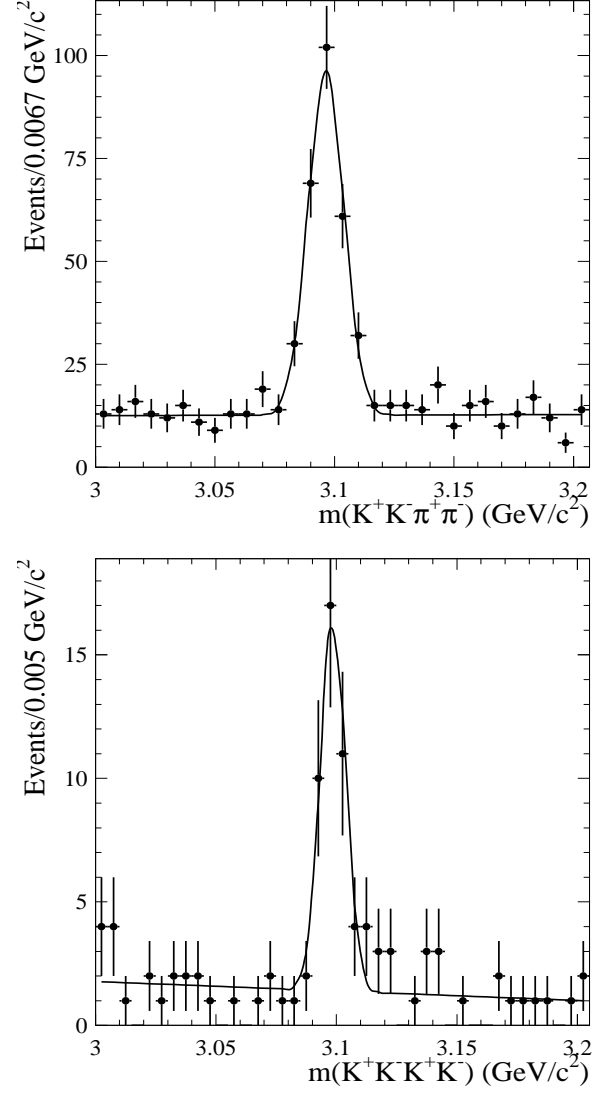


FIG. 27: The $K^+K^-\pi^+\pi^-$ (top) and $K^+K^-K^+K^-$ (bottom) mass distributions for ISR-produced events in the J/ψ region. A clear signal is observed at the J/ψ mass.

The $\psi(2S)$ peak corresponds to the decay chain $\psi(2S) \rightarrow J/\psi\pi^+\pi^- \rightarrow \mu^+\mu^-\pi^+\pi^-$ with the muons treated as pions. The number of events extracted from a fit to a Gaussian distribution for the $\psi(2S)$ peak and a polynomial function for the continuum is 544 ± 27 . With a radiative correction of 0.89 taken from simulation, $N(\psi(2S) \rightarrow J/\psi\pi^+\pi^-) = 611 \pm 30$ events is the observed signal.

The number of $\psi(2S)$ events can be obtained with much less background if the invariant mass of one pair of charged tracks assumed to be muons is within $\pm 50 \text{ MeV}/c^2$ of the J/ψ mass. Events satisfying this criterion are shown by the shaded histogram in Fig. 26; this $\psi(2S)$ peak has 620 ± 25 events after subtraction of 10 background events. With this number and the 544 ± 27 events obtained from the Gaussian fit, the radia-

tive correction value can be obtained directly; the value is 0.877 ± 0.013 , in good agreement with the value 0.89 from simulation.

For the $\psi(2S)$ we then obtain:

$$\begin{aligned} & B_{\psi(2S) \rightarrow J/\psi \pi^+ \pi^-} \cdot B_{J/\psi \rightarrow \mu^+ \mu^-} \cdot \sigma_{\text{int}}^{\psi(2S)} \\ &= \frac{N(\psi(2S) \rightarrow J/\psi \pi^+ \pi^-)}{d\mathcal{L}/dE \cdot \epsilon_{\text{MC}}} \\ &= 76.3 \pm 3.1 \pm 3.8 \text{ nb MeV} \end{aligned}$$

which leads to

$$\begin{aligned} & B_{\psi(2S) \rightarrow J/\psi \pi^+ \pi^-} \cdot B_{J/\psi \rightarrow \mu^+ \mu^-} \cdot \Gamma_{ee}^{\psi(2S)} \\ &= \frac{N(\psi(2S) \rightarrow J/\psi \pi^+ \pi^-) \cdot m_{\psi(2S)}^2}{6 \cdot \pi^2 \cdot d\mathcal{L}/dE \cdot \epsilon_{\text{MC}} \cdot C} \\ &= (4.50 \pm 0.18 \pm 0.22) \times 10^{-2} \text{ keV} , \end{aligned}$$

where $d\mathcal{L}/dE = 32.4 \text{ nb}^{-1}/\text{MeV}$ is the ISR luminosity at the $\psi(2S)$ mass, and $\epsilon_{\text{MC}} = 0.25 \pm 0.01$ is the detection efficiency from simulation with corrections discussed in Sec. IV F. The same systematic errors as for the J/ψ have been included.

Using the values $\Gamma_{ee}^{\psi(2S)} = 2.12 \pm 0.12 \text{ keV}$ and $B_{J/\psi \rightarrow \mu^+ \mu^-} = 0.0588 \pm 0.0010$ from Ref. [17], we obtain

$$B_{\psi(2S) \rightarrow J/\psi \pi^+ \pi^-} = 0.361 \pm 0.015 \pm 0.028 ,$$

which should be compared to the current world-average value, $B_{\psi(2S) \rightarrow J/\psi \pi^+ \pi^-} = 0.317 \pm 0.011$ [17]. Almost half of our systematic error in $B_{\psi(2S) \rightarrow J/\psi \pi^+ \pi^-}$ comes from the uncertainty in $\Gamma_{ee}^{\psi(2S)}$.

Alternatively, using the PDG values for the two branching fractions, we can extract the e^+e^- width of the $\psi(2S)$,

$$\Gamma_{ee}^{\psi(2S)} = 2.41 \pm 0.10 \pm 0.15 \text{ keV} ,$$

where the systematic error has been increased due to the uncertainty in $B_{\psi(2S) \rightarrow J/\psi \pi^+ \pi^-}$.

Figure 27 shows the J/ψ signal in the $K^+K^-\pi^+\pi^-$ and $K^+K^-K^+K^-$ modes. The numbers of events under the Gaussian curves are 233 ± 19 and 38.5 ± 6.7 respectively. The mass resolution is about $7 \text{ MeV}/c^2$ for $2K2\pi$ and $5 \text{ MeV}/c^2$ for the $4K$ final state. Using the radiative correction factor 0.877, and $\epsilon_{2K2\pi} = 0.13 \pm 0.01$ and $\epsilon_{4K} = 0.18 \pm 0.02$ from simulation, we obtain

$$\begin{aligned} B_{J/\psi \rightarrow 2K2\pi} \cdot \Gamma_{ee}^{J/\psi} &= (3.36 \pm 0.27 \pm 0.27) \times 10^{-2} \text{ keV} \\ B_{J/\psi \rightarrow 4K} \cdot \Gamma_{ee}^{J/\psi} &= (4.0 \pm 0.7 \pm 0.6) \times 10^{-3} \text{ keV} . \end{aligned}$$

The systematic errors are mainly due to the uncertainties in acceptance and ISR luminosity.

Using the PDG value for $\Gamma_{ee}^{J/\psi}$, we calculate the branching fractions

$$\begin{aligned} B_{J/\psi \rightarrow 2K2\pi} &= (6.2 \pm 0.5 \pm 0.5) \times 10^{-3} \\ B_{J/\psi \rightarrow 4K} &= (7.4 \pm 1.2 \pm 1.2) \times 10^{-4} , \end{aligned}$$

to be compared with the current PDG values of $(7.2 \pm 2.3) \cdot 10^{-3}$ and $(9.2 \pm 3.3) \cdot 10^{-4}$ respectively. The uncertainty in $\Gamma_{ee}^{J/\psi}$ has been added in quadrature to the systematic error estimate.

Since we have measured the products of $\sigma_{\text{int}}^{J/\psi}$ and branching fraction of J/ψ decay to 4π , $2K2\pi$, and $4K$ it is interesting to compare them with the non-resonant cross sections (continuum) at that energy. Using a linear approximation of the cross sections from Tables III, IV, V around the J/ψ peak within $\pm 0.1 \text{ GeV}$ (events from the peak are excluded), the following cross sections are obtained at the J/ψ mass:

$$\begin{aligned} \sigma_{4\pi} &= 0.55 \pm 0.03 \text{ nb} \\ \sigma_{2K2\pi} &= 0.48 \pm 0.04 \text{ nb} \\ \sigma_{4K} &= 0.055 \pm 0.009 \text{ nb} . \end{aligned}$$

Table II presents the ratios $B_{J/\psi \rightarrow f} \cdot \sigma_{\text{int}}^{J/\psi} / \sigma_{e^+e^- \rightarrow f}$ for $f = 4\pi, 2K2\pi, 4K$. In these ratios all experimental systematic errors cancel. Also shown is the ratio $B_{J/\psi \rightarrow \mu^+ \mu^-} \cdot \sigma_{\text{int}}^{J/\psi} / \sigma_{e^+e^- \rightarrow \mu^+ \mu^-}$ taken from Ref. [7].

TABLE II: Ratios of the J/ψ partial production rates to continuum cross sections. The result for $\mu^+\mu^-$ is from Ref. [7].

Final state, f	$B_{J/\psi \rightarrow f} \cdot \sigma_{\text{int}}^{J/\psi} / \sigma_{e^+e^- \rightarrow f} \text{ (MeV)}$
$\pi^+\pi^-\pi^+\pi^-$	85.1 ± 7.9
$K^+K^-\pi^+\pi^-$	166 ± 19
$K^+K^-K^+K^-$	138 ± 32
$\mu^+\mu^-$	84.12 ± 0.67

The ratio obtained for the 4π final state is in good agreement with that for $\mu^+\mu^-$. Indeed, the strong decay of the J/ψ to 4π is forbidden by G-parity conservation and therefore this decay is expected to be dominated by single-photon. No such suppression due to G-parity for the strong decay of the J/ψ for the other two modes. We interpret the significantly larger values of the ratios as an indication that the single-photon mechanism is not dominant for the J/ψ decays to the $2K2\pi$ and $4K$ final states.

VIII. THE SEARCH FOR THE $X(3872)$

Events in the J/ψ mass region can be used to search for the new narrow $X(3872)$ state reported by Belle [26]. If this state has $J^{PC} = 1^{--}$ it could be seen in ISR production via the decay to $J/\psi \pi^+ \pi^-$, just as for the $\psi(2S)$ (see Fig. 26). We acknowledge that such a J^{PC} assignment is improbable since it would permit the unobserved decay to $D\bar{D}$, which would make the $X(3872)$ much broader. If the J/ψ is selected in its decay to two muons, this state can be searched for as a peak at $3872 \text{ MeV}/c^2$ in the four-charged-track sample. Using our ISR data, we can set an upper limit on the product $B_{X \rightarrow J/\psi \pi^+ \pi^-} \cdot \Gamma_{ee}^X$. To improve background rejection, we

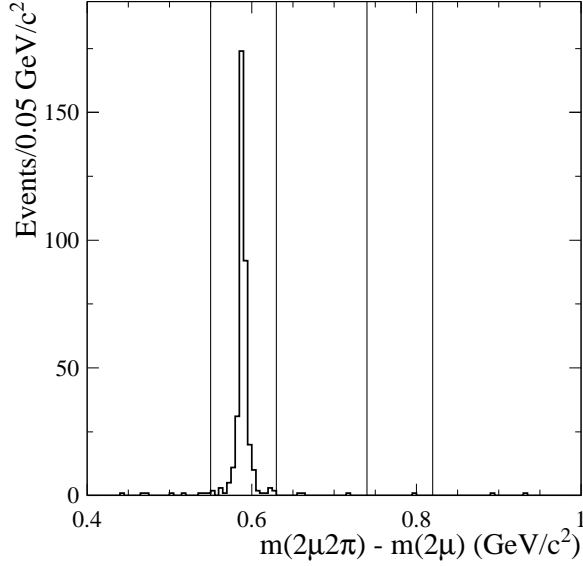


FIG. 28: The $m(2\mu 2\pi) - m(2\mu)$ difference for events with $m(2\mu)$ near the J/ψ mass and both particles identified as muons. The lines show the $\psi(2S)$ and $X(3872)$ selection regions.

require positive muon identification on two tracks, in addition to having the invariant mass of the two muons fall in the interval $[3.05\text{--}3.15]$ GeV/c^2 . Figure 28 displays the difference between the mass of the four-track final state and that of the two muons. The vertical lines show the selected regions for those events from $\psi(2S)$ decay and for the $X(3872)$ search. The number of events within the $\psi(2S)$ interval is used to estimate the di-muon identification efficiency, which is found to be 0.61 for this study. Events in the interval $[0.65\text{--}1.0]$ GeV/c^2 are used to estimate the background within the expected region for $X(3872)$ decay, namely $[0.74\text{--}0.82]$ GeV/c^2 . One event is found within this interval where 1.4 are expected from background; this yields an upper limit of 3.0 events at the 90% confidence level. From this limit an upper limit on the product of the branching fraction of the $X(3872)$ to $J/\psi\pi^+\pi^-$ and the e^+e^- width of $X(3872)$ is obtained through the chain

$$B_{X \rightarrow J/\psi\pi^+\pi^-} \cdot B_{J/\psi \rightarrow 2\mu} \cdot \Gamma_{ee}^X = \frac{N(X \rightarrow J/\psi\pi^+\pi^-) \cdot m_X^2}{6 \cdot \pi^2 \cdot d\mathcal{L}/dE \cdot \epsilon_{\text{MC}} \cdot C \cdot 0.61} < 0.37 \text{ eV}, \quad (6)$$

where $d\mathcal{L}/dE = 34.7 \text{ nb}^{-1}/\text{MeV}$ is the ISR luminosity at the $X(3872)$ mass, and $\epsilon_{\text{MC}} = 0.25 \pm 0.01$ is the acceptance from simulation.

Using the value $B_{J/\psi \rightarrow 2\mu} = 0.0588 \pm 0.0010$ [17], we extract the upper limit

$$B_{X(3872) \rightarrow J/\psi\pi^+\pi^-} \cdot \Gamma_{ee}^X < 6.2 \text{ eV at 90\% C.L.}$$

This result is the best upper limit to date and can be compared with the result of a similar study performed by BES [27].

IX. SUMMARY

The photon energy and charged particle momentum resolutions together with the particle identification capabilities of the *BABAR* detector permit the reconstruction of $\pi^+\pi^-\pi^+\pi^-$, $K^+K^-\pi^+\pi^-$ and $K^+K^-K^+K^-$ final states produced at low effective c.m. energy via ISR in data taken in the $\Upsilon(4S)$ mass region.

The analysis shows that luminosity and efficiency can be understood with 2–4% accuracy, and that ISR production yields useful measurements of R , the ratio of the hadronic to di-muon cross section values, in the low-energy regime of e^+e^- collisions.

The selected multi-hadronic final states in the broad range of accessible energy provide new information on hadron spectroscopy. The observed $e^+e^- \rightarrow \pi^+\pi^-\pi^+\pi^-$ cross section provides evidence of resonant structure, with preferred quasi-two-body production of $a_1(1260)\pi$. For the first time there is an indication of a $f_0(1370)\rho(770)$ contribution to the final state. However a detailed understanding of the four-pion final state requires additional information from states such as $\pi^+\pi^-\pi^0\pi^0$.

The cross section measurements for the reaction $e^+e^- \rightarrow K^+K^- \pi^+\pi^-$ present a significant improvement upon existing data with about 15% systematic uncertainty. In addition, the final state exhibits complex resonance sub-structure. Clear signals for $K^{*0}(892)$, ϕ , and ρ are observed; there is evidence of $K_2^*(1430)$ production; and there are low-mass enhancements in the $K^{*0}(892)K^\pm$, $K^{*0}(892)\pi$, $\phi\pi$, and $K\rho$ subsystems. It is difficult to disentangle these contributions to the final state, and we make no attempt to do so in this paper.

The energy dependence of the cross section for the reaction $e^+e^- \rightarrow K^+K^-K^+K^-$ from threshold to 4.5 GeV has been measured for the first time with about 20% systematic uncertainty. In contrast to the $K^+K^-\pi^+\pi^-$ final state, the four-kaon state shows no clear mass structure in the two- and three-body sub-systems. The absence of a clear ϕ signal in the K^+K^- mass distribution is unexpected.

The analyzed 89 fb^{-1} of *BABAR* data in the 1.4–4.5 GeV/c^2 mass range are already better in quality and precision than the direct measurements from the DCI and ADONE machines, and do not suffer from the relative normalization uncertainties which seem to exist for direct measurements of these final states.

The ISR events allow a study of J/ψ and $\psi(2S)$ production, and the measurement of the product of decay branching fractions and e^+e^- width of the J/ψ with the

best accuracy to date. The results are as follows:

$$\begin{aligned}
& B_{J/\psi \rightarrow 4\pi} \cdot \Gamma_{ee}^{J/\psi} \\
&= (1.95 \pm 0.14 \pm 0.13) \times 10^{-2} \text{ keV} , \\
& B_{\psi(2S) \rightarrow J/\psi \pi^+ \pi^-} \cdot B_{J/\psi \rightarrow 2\mu} \cdot \Gamma_{ee}^{\psi(2S)} \\
&= (4.50 \pm 0.18 \pm 0.22) \times 10^{-2} \text{ keV} , \\
& B_{J/\psi \rightarrow 2K2\pi} \cdot \Gamma_{ee}^{J/\psi} \\
&= (3.36 \pm 0.27 \pm 0.27) \times 10^{-2} \text{ keV} , \\
& B_{J/\psi \rightarrow 4K} \cdot \Gamma_{ee}^{J/\psi} \\
&= (4.0 \pm 0.7 \pm 0.6) \times 10^{-3} \text{ keV} .
\end{aligned}$$

The dominance of the single-photon-decay mechanism for $J/\psi \rightarrow \pi^+ \pi^- \pi^+ \pi^-$ has been demonstrated by comparison with the continuum cross section $e^+ e^- \rightarrow \pi^+ \pi^- \pi^+ \pi^-$.

Under the assumption that the $X(3872)$ has $J^{PC} = 1^{--}$, we have obtained the best upper limit to date on the product of its branching fraction to $J/\psi \pi^+ \pi^-$ and its $e^+ e^-$ width:

$$B_{X(3872) \rightarrow J/\psi \pi^+ \pi^-} \cdot \Gamma_{ee}^X < 6.2 \text{ eV at 90\% CL.}$$

X. ACKNOWLEDGMENTS

The authors wish to thank Prof. J. H. Kuehn and H. Czyz for developing the Monte Carlo generator for ISR

processes which was incorporated into *BABAR* analysis system.

We are grateful for the extraordinary contributions of our PEP-II colleagues in achieving the excellent luminosity and machine conditions that have made this work possible. The success of this project also relies critically on the expertise and dedication of the computing organizations that support *BABAR*. The collaborating institutions wish to thank SLAC for its support and the kind hospitality extended to them. This work is supported by the US Department of Energy and National Science Foundation, the Natural Sciences and Engineering Research Council (Canada), Institute of High Energy Physics (China), the Commissariat à l’Energie Atomique and Institut National de Physique Nucléaire et de Physique des Particules (France), the Bundesministerium für Bildung und Forschung and Deutsche Forschungsgemeinschaft (Germany), the Istituto Nazionale di Fisica Nucleare (Italy), the Foundation for Fundamental Research on Matter (The Netherlands), the Research Council of Norway, the Ministry of Science and Technology of the Russian Federation, and the Particle Physics and Astronomy Research Council (United Kingdom). Individuals have received support from CONACyT (Mexico), the A. P. Sloan Foundation, the Research Corporation, and the Alexander von Humboldt Foundation.

-
- [1] V. N. Baier and V. S. Fadin, Phys. Lett. **B27**, 223 (1968).
 - [2] A. B. Arbuzov *et al.*, J. High Energy Phys. **9812**, 009 (1998).
 - [3] S. Binner, J.H. Kuehn and K. Melnikov, Phys. Lett. **B459**, 279(1999).
 - [4] M. Benayoun *et al.*, Mod. Phys. Lett. **A14**, 2605 (1999).
 - [5] M. Davier, S. Eidelman, A. Hocker, Z. Zhang, Eur. Phys. J. **C31**, 503 (2003).
 - [6] E.P.Solodov (for *BABAR* Collaboration). “Study of $e^+ e^-$ collisions in the 1.5-3.0 GeV C.M. Energy Region Using ISR at *BABAR*”, Invited talk at “International Workshop on $e^+ e^-$ Physics at Intermediate Energy”, SLAC, Stanford, April 30-May 4, 2001, hep-ex/0107027.
 - [7] *BABAR* Collaboration, B. Aubert *et al.*, Phys. Rev. **D69**, 011103 (2004).
 - [8] *BABAR* Collaboration, B. Aubert *et al.*, Phys. Rev. **D70**, 072004 (2004).
 - [9] *BABAR* Collaboration, B. Aubert *et al.*, Nucl. Instrum. Methods Phys. Research **A479**, 1 (2002).
 - [10] H. Czyz and J. H. Kuehn, Eur. Phys. J. **C18**, 497 (2001).
 - [11] A. B. Arbuzov *et al.*, J. High Energy Phys. **9710**, 001 (1997).
 - [12] M. Caffo, H. Czyz, E. Remiddi, Nuovo Cim. **A110**, 515 (1997); Phys. Lett. **B327**, 369 (1994).
 - [13] E. Barberio, B. van Eijk and Z. Was, Comput. Phys. Commun. **66**, 115 (1991).
 - [14] The *BABAR* detector Monte Carlo simulation is based on GEANT4: S. Agostinelli *et al.*, Nucl. Instr. Methods Phys. Res., Sect. A **506**, 250 (2003).
 - [15] T. Sjostrand, Comput. Phys. Commun. **82**, 74 (1994).
 - [16] S. Jadach and Z. Was, Comput. Phys. Commun. **85**, 453 (1995).
 - [17] Review of Particle Physics, S. Eidelman *et al.*, Phys. Lett. **B592**, 1 (2004).
 - [18] CMD-2 Collaboration, R. R. Akhmetshin *et al.*, Phys. Lett. **B595**, 101 (2004).
 - [19] A. Bondar *et al.*, Phys. Lett. **B466**, 403 (1999).
 - [20] S. Eidelman and F. Jegerlehner, Z. Phys. **C67**, 585 (1995).
 - [21] SND Collaboration, M. N. Achasov *et al.*, J. Exp. Theor. Phys. **96**, 789 (2003).
 - [22] CMD-2 Collaboration, R. R. Akhmetshin *et al.*, Phys. Lett. **B475**, 190 (2000).
 - [23] D. Bisello *et al.*, Nucl. Phys. B (Proc. Suppl.) **21**, 111 (1991).
 - [24] CLEO Collaboration, A. J. Weinstein *et al.*, Nucl. Phys. B (Proc. Suppl.) **98**, 261 (2001).
 - [25] A. Cordier *et al.*, Phys. Lett. **B110**, 335 (1982).
 - [26] Belle Collaboration, S. K. Choi *et al.*, Phys. Rev. Lett. **91**, 262001 (2003).
 - [27] J. Z. Bai *et al.*, Phys. Rev. **D57**, 3854 (1998).

TABLE III: Summary of $e^+e^- \rightarrow \pi^+\pi^-\pi^+\pi^-$ cross section measurement. "Dressed" and "Undressed" (without vacuum polarization) cross sections are presented. Errors are statistical only.

$E_{c.m.}$ (GeV)	σ (nb)	σ_{noVP} (nb)	$E_{c.m.}$ (GeV)	σ (nb)	σ_{noVP} (nb)	$E_{c.m.}$ (GeV)	σ (nb)	σ_{noVP} (nb)
0.6125	0.00 ± 0.19	0.00 ± 0.19	1.8125	10.06 ± 0.40	9.68 ± 0.38	3.0125	0.61 ± 0.10	0.60 ± 0.10
0.6375	0.22 ± 0.13	0.22 ± 0.13	1.8375	8.29 ± 0.37	7.98 ± 0.36	3.0375	0.85 ± 0.10	0.84 ± 0.10
0.6625	0.07 ± 0.16	0.07 ± 0.16	1.8625	6.99 ± 0.33	6.73 ± 0.32	3.0625	0.58 ± 0.09	0.59 ± 0.09
0.6875	0.09 ± 0.07	0.09 ± 0.07	1.8875	6.86 ± 0.33	6.60 ± 0.32	3.0875	1.53 ± 0.13	0.43 ± 0.04
0.7125	0.00 ± 0.00	0.00 ± 0.00	1.9125	6.23 ± 0.32	6.00 ± 0.31	3.1125	1.02 ± 0.12	0.78 ± 0.09
0.7375	0.07 ± 0.05	0.07 ± 0.05	1.9375	6.55 ± 0.31	6.31 ± 0.30	3.1375	0.31 ± 0.08	0.28 ± 0.07
0.7625	0.03 ± 0.03	0.03 ± 0.03	1.9625	6.29 ± 0.31	6.06 ± 0.30	3.1625	0.44 ± 0.09	0.41 ± 0.08
0.7875	0.06 ± 0.08	0.06 ± 0.08	1.9875	5.92 ± 0.31	5.70 ± 0.30	3.1875	0.44 ± 0.08	0.41 ± 0.07
0.8125	0.08 ± 0.05	0.08 ± 0.05	2.0125	5.48 ± 0.30	5.28 ± 0.29	3.2125	0.51 ± 0.08	0.48 ± 0.08
0.8375	0.11 ± 0.08	0.10 ± 0.08	2.0375	5.72 ± 0.29	5.51 ± 0.28	3.2375	0.23 ± 0.07	0.22 ± 0.07
0.8625	0.28 ± 0.09	0.27 ± 0.09	2.0625	5.38 ± 0.28	5.18 ± 0.27	3.2625	0.29 ± 0.07	0.27 ± 0.07
0.8875	0.37 ± 0.09	0.35 ± 0.09	2.0875	5.50 ± 0.28	5.29 ± 0.27	3.2875	0.29 ± 0.08	0.27 ± 0.08
0.9125	0.44 ± 0.11	0.42 ± 0.11	2.1125	4.60 ± 0.26	4.43 ± 0.25	3.3125	0.37 ± 0.08	0.35 ± 0.08
0.9375	0.36 ± 0.11	0.35 ± 0.11	2.1375	4.78 ± 0.26	4.60 ± 0.25	3.3375	0.35 ± 0.08	0.33 ± 0.08
0.9625	0.78 ± 0.14	0.76 ± 0.14	2.1625	4.73 ± 0.26	4.55 ± 0.25	3.3625	0.31 ± 0.07	0.29 ± 0.07
0.9875	0.94 ± 0.16	0.92 ± 0.16	2.1875	3.82 ± 0.24	3.68 ± 0.23	3.3875	0.31 ± 0.07	0.29 ± 0.07
1.0125	1.14 ± 0.17	1.13 ± 0.17	2.2125	3.49 ± 0.24	3.36 ± 0.23	3.4125	0.31 ± 0.07	0.30 ± 0.07
1.0375	1.76 ± 0.20	1.64 ± 0.19	2.2375	3.55 ± 0.23	3.42 ± 0.22	3.4375	0.09 ± 0.07	0.09 ± 0.07
1.0625	2.65 ± 0.22	2.52 ± 0.21	2.2625	3.43 ± 0.23	3.30 ± 0.22	3.4625	0.23 ± 0.07	0.22 ± 0.07
1.0875	3.07 ± 0.25	2.93 ± 0.24	2.2875	3.11 ± 0.23	2.99 ± 0.22	3.4875	0.31 ± 0.06	0.30 ± 0.06
1.1125	3.82 ± 0.28	3.66 ± 0.27	2.3125	2.69 ± 0.20	2.59 ± 0.19	3.5125	0.26 ± 0.06	0.25 ± 0.06
1.1375	5.02 ± 0.33	4.82 ± 0.32	2.3375	3.13 ± 0.21	3.01 ± 0.20	3.5375	0.14 ± 0.06	0.13 ± 0.06
1.1625	7.10 ± 0.37	6.83 ± 0.36	2.3625	2.51 ± 0.19	2.42 ± 0.18	3.5625	0.13 ± 0.06	0.12 ± 0.06
1.1875	7.97 ± 0.39	7.67 ± 0.38	2.3875	2.11 ± 0.19	2.03 ± 0.18	3.5875	0.12 ± 0.06	0.12 ± 0.06
1.2125	10.56 ± 0.45	10.17 ± 0.43	2.4125	2.30 ± 0.18	2.21 ± 0.17	3.6125	0.12 ± 0.05	0.12 ± 0.05
1.2375	12.30 ± 0.47	11.86 ± 0.45	2.4375	1.94 ± 0.18	1.87 ± 0.17	3.6375	0.09 ± 0.06	0.09 ± 0.06
1.2625	13.48 ± 0.51	13.00 ± 0.49	2.4625	2.18 ± 0.16	2.10 ± 0.15	3.6625	0.00 ± 0.06	0.00 ± 0.06
1.2875	16.02 ± 0.53	15.46 ± 0.51	2.4875	1.76 ± 0.17	1.69 ± 0.16	3.6875	0.12 ± 0.05	0.10 ± 0.04
1.3125	18.27 ± 0.57	17.64 ± 0.55	2.5125	1.73 ± 0.16	1.67 ± 0.15	3.7125	0.06 ± 0.05	0.06 ± 0.05
1.3375	20.27 ± 0.60	19.57 ± 0.58	2.5375	1.62 ± 0.17	1.56 ± 0.16	3.7375	0.11 ± 0.05	0.10 ± 0.05
1.3625	21.70 ± 0.61	20.97 ± 0.59	2.5625	1.69 ± 0.15	1.63 ± 0.14	3.7625	0.22 ± 0.06	0.21 ± 0.06
1.3875	24.90 ± 0.66	24.06 ± 0.64	2.5875	1.49 ± 0.15	1.43 ± 0.14	3.7875	0.08 ± 0.05	0.08 ± 0.05
1.4125	27.05 ± 0.67	26.16 ± 0.65	2.6125	1.50 ± 0.15	1.44 ± 0.14	3.8125	0.12 ± 0.05	0.11 ± 0.05
1.4375	28.33 ± 0.68	27.37 ± 0.66	2.6375	1.33 ± 0.15	1.28 ± 0.14	3.8375	0.04 ± 0.05	0.04 ± 0.05
1.4625	29.32 ± 0.70	28.33 ± 0.68	2.6625	1.24 ± 0.13	1.19 ± 0.12	3.8625	0.10 ± 0.05	0.09 ± 0.05
1.4875	30.20 ± 0.72	29.18 ± 0.70	2.6875	1.07 ± 0.13	1.03 ± 0.12	3.8875	0.13 ± 0.05	0.12 ± 0.05
1.5125	29.82 ± 0.70	28.78 ± 0.68	2.7125	1.01 ± 0.13	0.97 ± 0.12	3.9125	0.17 ± 0.04	0.16 ± 0.04
1.5375	28.77 ± 0.67	27.77 ± 0.65	2.7375	0.94 ± 0.13	0.90 ± 0.13	3.9375	0.08 ± 0.05	0.08 ± 0.05
1.5625	26.43 ± 0.65	25.51 ± 0.63	2.7625	1.01 ± 0.12	0.97 ± 0.12	3.9625	0.06 ± 0.05	0.06 ± 0.05
1.5875	26.03 ± 0.63	25.13 ± 0.61	2.7875	1.05 ± 0.12	1.01 ± 0.12	3.9875	0.07 ± 0.05	0.07 ± 0.05
1.6125	22.93 ± 0.61	22.13 ± 0.59	2.8125	0.88 ± 0.11	0.85 ± 0.11	4.0125	0.05 ± 0.05	0.05 ± 0.05
1.6375	22.05 ± 0.59	21.28 ± 0.57	2.8375	0.86 ± 0.12	0.83 ± 0.12	4.0375	0.07 ± 0.04	0.07 ± 0.04
1.6625	19.84 ± 0.57	19.13 ± 0.55	2.8625	0.75 ± 0.11	0.72 ± 0.11	4.0625	0.08 ± 0.04	0.08 ± 0.04
1.6875	17.79 ± 0.52	17.16 ± 0.50	2.8875	0.77 ± 0.11	0.74 ± 0.11	4.0875	0.08 ± 0.04	0.08 ± 0.04
1.7125	16.22 ± 0.50	15.63 ± 0.48	2.9125	0.81 ± 0.12	0.78 ± 0.12	4.1500	0.03 ± 0.02	0.03 ± 0.02
1.7375	14.98 ± 0.48	14.43 ± 0.46	2.9375	0.51 ± 0.11	0.49 ± 0.11	4.2500	0.01 ± 0.02	0.01 ± 0.02
1.7625	12.92 ± 0.45	12.44 ± 0.43	2.9625	0.59 ± 0.10	0.57 ± 0.10	4.3500	0.02 ± 0.02	0.02 ± 0.02
1.7875	10.75 ± 0.42	10.35 ± 0.40	2.9875	0.64 ± 0.10	0.62 ± 0.10	4.4500	0.00 ± 0.02	0.00 ± 0.02

TABLE IV: Summary of $e^+e^- \rightarrow K^+K^-\pi^+\pi^-$ cross section measurement. "Dressed" and "Undressed" (without vacuum polarization) cross sections are presented. Errors are statistical only.

$E_{c.m.}$ (GeV)	σ (nb)	σ_{noVP} (nb)	$E_{c.m.}$ (GeV)	σ (nb)	σ_{noVP} (nb)	$E_{c.m.}$ (GeV)	σ (nb)	σ_{noVP} (nb)
1.5125	0.00 ± 0.00	0.00 ± 0.00	2.5125	1.27 ± 0.19	1.22 ± 0.18	3.5125	0.33 ± 0.07	0.32 ± 0.07
1.5375	0.03 ± 0.05	0.03 ± 0.05	2.5375	1.20 ± 0.18	1.15 ± 0.17	3.5375	0.29 ± 0.07	0.28 ± 0.07
1.5625	0.11 ± 0.05	0.11 ± 0.05	2.5625	1.58 ± 0.19	1.52 ± 0.18	3.5625	0.22 ± 0.06	0.21 ± 0.06
1.5875	0.29 ± 0.08	0.28 ± 0.08	2.5875	1.22 ± 0.17	1.17 ± 0.16	3.5875	0.07 ± 0.06	0.07 ± 0.06
1.6125	0.58 ± 0.13	0.56 ± 0.13	2.6125	1.02 ± 0.16	0.98 ± 0.15	3.6125	0.08 ± 0.05	0.08 ± 0.05
1.6375	0.96 ± 0.15	0.93 ± 0.14	2.6375	1.03 ± 0.16	0.99 ± 0.15	3.6375	0.08 ± 0.05	0.08 ± 0.05
1.6625	1.22 ± 0.19	1.18 ± 0.18	2.6625	0.83 ± 0.17	0.80 ± 0.16	3.6625	0.16 ± 0.06	0.16 ± 0.06
1.6875	1.60 ± 0.22	1.54 ± 0.21	2.6875	0.69 ± 0.14	0.66 ± 0.13	3.6875	0.21 ± 0.07	0.17 ± 0.06
1.7125	1.78 ± 0.25	1.71 ± 0.24	2.7125	1.18 ± 0.17	1.13 ± 0.16	3.7125	0.24 ± 0.07	0.22 ± 0.06
1.7375	2.67 ± 0.30	2.57 ± 0.29	2.7375	0.67 ± 0.15	0.64 ± 0.14	3.7375	0.11 ± 0.06	0.10 ± 0.06
1.7625	2.81 ± 0.33	2.70 ± 0.32	2.7625	0.98 ± 0.14	0.94 ± 0.13	3.7625	0.23 ± 0.06	0.22 ± 0.06
1.7875	2.99 ± 0.34	2.88 ± 0.33	2.7875	0.78 ± 0.14	0.75 ± 0.13	3.7875	0.13 ± 0.05	0.12 ± 0.05
1.8125	3.72 ± 0.36	3.58 ± 0.35	2.8125	0.72 ± 0.13	0.69 ± 0.13	3.8125	0.06 ± 0.05	0.06 ± 0.05
1.8375	4.16 ± 0.40	4.00 ± 0.38	2.8375	0.77 ± 0.13	0.74 ± 0.13	3.8375	0.13 ± 0.06	0.12 ± 0.06
1.8625	4.58 ± 0.41	4.41 ± 0.39	2.8625	0.63 ± 0.13	0.61 ± 0.13	3.8625	0.08 ± 0.06	0.08 ± 0.06
1.8875	4.34 ± 0.41	4.18 ± 0.39	2.8875	0.28 ± 0.12	0.27 ± 0.12	3.8875	0.08 ± 0.05	0.08 ± 0.05
1.9125	4.18 ± 0.38	4.03 ± 0.37	2.9125	0.48 ± 0.13	0.46 ± 0.13	3.9125	0.07 ± 0.04	0.07 ± 0.04
1.9375	4.70 ± 0.42	4.53 ± 0.40	2.9375	0.53 ± 0.11	0.51 ± 0.11	3.9375	0.07 ± 0.05	0.07 ± 0.05
1.9625	4.01 ± 0.38	3.86 ± 0.37	2.9625	0.44 ± 0.12	0.43 ± 0.12	3.9625	0.10 ± 0.05	0.10 ± 0.05
1.9875	4.11 ± 0.38	3.96 ± 0.37	2.9875	0.54 ± 0.11	0.53 ± 0.11	3.9875	0.03 ± 0.05	0.03 ± 0.05
2.0125	3.08 ± 0.33	2.97 ± 0.32	3.0125	0.48 ± 0.12	0.47 ± 0.12	4.0125	0.04 ± 0.04	0.04 ± 0.04
2.0375	3.19 ± 0.33	3.07 ± 0.32	3.0375	0.39 ± 0.11	0.39 ± 0.11	4.0375	0.13 ± 0.05	0.12 ± 0.05
2.0625	3.32 ± 0.35	3.20 ± 0.34	3.0625	0.46 ± 0.11	0.47 ± 0.11	4.0625	0.00 ± 0.00	0.00 ± 0.00
2.0875	2.79 ± 0.32	2.69 ± 0.31	3.0875	2.40 ± 0.24	0.67 ± 0.07	4.0875	0.02 ± 0.04	0.02 ± 0.04
2.1125	3.31 ± 0.32	3.19 ± 0.31	3.1125	1.30 ± 0.17	1.00 ± 0.13	4.1125	0.05 ± 0.04	0.05 ± 0.04
2.1375	2.84 ± 0.32	2.73 ± 0.31	3.1375	0.59 ± 0.11	0.53 ± 0.10	4.1375	0.00 ± 0.04	0.00 ± 0.04
2.1625	2.48 ± 0.28	2.39 ± 0.27	3.1625	0.48 ± 0.11	0.44 ± 0.10	4.1625	0.04 ± 0.04	0.04 ± 0.04
2.1875	2.83 ± 0.30	2.72 ± 0.29	3.1875	0.32 ± 0.10	0.30 ± 0.09	4.1875	0.04 ± 0.05	0.04 ± 0.05
2.2125	2.00 ± 0.25	1.92 ± 0.24	3.2125	0.57 ± 0.11	0.54 ± 0.10	4.2125	0.06 ± 0.04	0.06 ± 0.04
2.2375	1.79 ± 0.24	1.72 ± 0.23	3.2375	0.46 ± 0.10	0.43 ± 0.09	4.2375	0.01 ± 0.04	0.01 ± 0.04
2.2625	2.18 ± 0.26	2.10 ± 0.25	3.2625	0.40 ± 0.09	0.38 ± 0.08	4.2625	0.13 ± 0.04	0.12 ± 0.04
2.2875	1.53 ± 0.23	1.47 ± 0.22	3.2875	0.32 ± 0.08	0.30 ± 0.08	4.2875	0.04 ± 0.04	0.04 ± 0.04
2.3125	1.91 ± 0.24	1.84 ± 0.23	3.3125	0.40 ± 0.09	0.38 ± 0.09	4.3125	0.02 ± 0.04	0.02 ± 0.04
2.3375	1.73 ± 0.24	1.67 ± 0.23	3.3375	0.25 ± 0.07	0.24 ± 0.07	4.3375	0.06 ± 0.03	0.06 ± 0.03
2.3625	1.77 ± 0.21	1.70 ± 0.20	3.3625	0.40 ± 0.09	0.38 ± 0.09	4.3625	0.00 ± 0.04	0.00 ± 0.04
2.3875	1.54 ± 0.22	1.48 ± 0.21	3.3875	0.24 ± 0.07	0.23 ± 0.07	4.3875	0.02 ± 0.04	0.02 ± 0.04
2.4125	2.01 ± 0.23	1.93 ± 0.22	3.4125	0.22 ± 0.08	0.21 ± 0.08	4.4125	0.05 ± 0.04	0.05 ± 0.04
2.4375	1.38 ± 0.20	1.33 ± 0.19	3.4375	0.00 ± 0.00	0.00 ± 0.00	4.4375	0.05 ± 0.03	0.05 ± 0.03
2.4625	1.61 ± 0.22	1.55 ± 0.21	3.4625	0.24 ± 0.08	0.23 ± 0.08	4.4625	0.05 ± 0.03	0.05 ± 0.03
2.4875	1.84 ± 0.21	1.77 ± 0.20	3.4875	0.21 ± 0.07	0.20 ± 0.07	4.4875	0.06 ± 0.04	0.06 ± 0.04

TABLE V: Summary of $e^+e^- \rightarrow K^+K^-K^+K^-$ cross section measurement. "Dressed" and "Undressed" (without vacuum polarization) cross sections are presented. Errors are statistical only.

$E_{c.m.}$ (GeV)	σ (nb)	σ_{noVP} (nb)	$E_{c.m.}$ (GeV)	σ (nb)	σ_{noVP} (nb)	$E_{c.m.}$ (GeV)	σ (nb)	σ_{noVP} (nb)
2.0312	0.00 ± 0.01	0.00 ± 0.00	2.9062	0.07 ± 0.02	0.06 ± 0.02	3.7188	0.00 ± 0.01	0.00 ± 0.01
2.0938	0.02 ± 0.01	0.02 ± 0.01	2.9688	0.08 ± 0.02	0.08 ± 0.02	3.7812	0.05 ± 0.01	0.04 ± 0.01
2.1562	0.05 ± 0.01	0.05 ± 0.01	3.0312	0.06 ± 0.02	0.06 ± 0.02	3.8438	0.03 ± 0.01	0.03 ± 0.01
2.2188	0.08 ± 0.02	0.08 ± 0.02	3.0938	0.19 ± 0.03	0.18 ± 0.03	3.9062	0.01 ± 0.01	0.01 ± 0.01
2.2812	0.07 ± 0.02	0.07 ± 0.02	3.1562	0.03 ± 0.02	0.03 ± 0.02	3.9688	0.01 ± 0.01	0.01 ± 0.01
2.3438	0.08 ± 0.02	0.07 ± 0.02	3.2188	0.05 ± 0.01	0.05 ± 0.01	4.0312	0.03 ± 0.01	0.03 ± 0.01
2.4062	0.07 ± 0.02	0.07 ± 0.02	3.2812	0.03 ± 0.01	0.03 ± 0.01	4.0938	0.01 ± 0.01	0.01 ± 0.01
2.4688	0.08 ± 0.03	0.08 ± 0.03	3.3438	0.04 ± 0.02	0.04 ± 0.02	4.1562	0.02 ± 0.01	0.02 ± 0.01
2.5312	0.05 ± 0.02	0.05 ± 0.02	3.4062	0.05 ± 0.02	0.05 ± 0.02	4.2188	0.04 ± 0.01	0.04 ± 0.01
2.5938	0.07 ± 0.02	0.07 ± 0.02	3.4688	0.03 ± 0.01	0.03 ± 0.01	4.2812	0.00 ± 0.01	0.00 ± 0.01
2.6562	0.10 ± 0.03	0.10 ± 0.02	3.5312	0.05 ± 0.01	0.05 ± 0.01	4.3438	0.01 ± 0.01	0.00 ± 0.01
2.7188	0.13 ± 0.03	0.12 ± 0.03	3.5938	0.02 ± 0.01	0.02 ± 0.01	4.4062	0.00 ± 0.01	0.00 ± 0.01
2.7812	0.08 ± 0.02	0.07 ± 0.02	3.6562	0.02 ± 0.01	0.02 ± 0.01	4.4688	0.00 ± 0.01	0.00 ± 0.01
2.8438	0.10 ± 0.02	0.09 ± 0.02						